Macrophage-derived insulin/IGF antagonist ImpL2 regulates systemic metabolism for mounting an effective acute immune response in *Drosophila*

Krejčová Gabriela[1#], Bajgar Adam[1#*], Nedbalová Pavla[1], Kovářová Julie[2], Kamps-Hughes Nick[3], Zemanová Helena[1], Strych Lukáš[1], Doležal Tomáš[1*]

[1]University of South Bohemia, Czech Republic, [2]Biology Centre CAS, Czech Republic, [3]University of Oregon, United States

[#]equal contribution

[*]For correspondence: AB - bajgaa00@prf.jcu.cz TD - tomas.dolezal@prf.jcu.cz

Abstract

In response to invading pathogens, macrophages metabolically polarize toward Hif1α-induced aerobic glycolysis, requiring increased supply of nutrients. Here, we show that in order to obtain sufficient resources, *Drosophila* macrophages release the insulin/IGF antagonist ImpL2 in a Hif1α-dependent manner as a reflection of adopted polarization. ImpL2 remotely induces Foxo-mediated lipid mobilization and the release of lipoproteins and carbohydrates from adipose tissue to be utilized by the activated immune system. Although these ImpL2 effects are essential in acute streptococcal infection, they become maladaptive during chronic intracellular *Listeria* infection. The relevance of our model to mammalian immuno-metabolism is documented by the increased expression of the ImpL2 homolog IGFBP7 in human macrophages exposed to *Streptococcus*. Therefore, we postulate that ImpL2/IGFBP7 induce resource mobilization, which is beneficial during the acute phase of infection but may act as cachectic factors in patients with cancer, sepsis, or obesity.

Keywords:

Macrophage, immuno-metabolism, Drosophila, immunity, bacterial infection, Streptococcus, ImpL2, IGFBP7, energy mobilization, Hif1α, aerobic glycolysis, macrophage polarization, insulin resistance, selfish immune system, adipose tissue remodeling, Foxo, infection-induced insulin resistance, Listeria, Insulin/IGF antagonist, wasting, cachexia

Introduction

Macrophages represent the front line in defence against invading pathogens. Although the effectiveness of the immune response correlates with the number of immune cells (Nicholson and Nicholson 2008), their maintenance requires energy and excessive activation can lead to a myriad of pathologies and metabolic disorders (Shattuck-Heidorn et al. 2016; Zmora et al. 2017). Animals have therefore developed a strategy that allows them to maintain a sufficient number of quiescent immune cells that can be rapidly activated in response to the detection of pathogen- or danger-associated molecular patterns (Kelly and O'Neill 2015). Numerous populations of sentinel macrophages wait for activation stimuli without being an energy burden. As a consequence, macrophages depend on rapid and sufficient supplementation from external sources, making the acute phase of the immune response challenging for the whole organism (Newsholme et al. 1986).

In response to recognition of the invading pathogen, macrophages must rapidly alter their metabolism to generate enough energy and precursors to support their bactericidal function. Therefore, bactericidal (M1) macrophages substantially increase the rate of glycolysis and the pentose phosphate pathway and rewire their mitochondrial metabolism in a Hif1α-dependent

manner (Van den Bossche, O'Neill, and Menon 2017). Such a metabolic setup resembles the Warburg effect originally described as a unique metabolic program for cancer cells (Warburg 1925). We have recently shown that the metabolic polarization of macrophages is an ancient and evolutionarily conserved process, since even *Drosophila* macrophages undergo a metabolic switch triggered by Hif1α, which is essential for their bactericidal function (Krejčová et al. 2019).

An adverse aspect of M1 polarization is that these cells require more energy and become functionally dependent on external sources of glucose, glutamine, and lipids. Therefore, in response to their metabolic activation, macrophages release signals that regulate systemic metabolism and thus ensure their supply of nutrients at the expense of other organs (Straub 2014). Such privileged behavior, in which macrophages usurp nutrients from other processes, is crucial for an effective immune response (Bajgar and Dolezal 2018). One of the factors mediating such behavior is extracellular adenosine, which links the current metabolic state of activated immune cells to the systemic mobilization of carbohydrates, which serve as a source for immune defense (Bajgar et al. 2015; Bajgar and Dolezal 2018). However, the response is very complex and we assume the existence of other signaling factors with an analogous function.

To discover other signaling factors that are released by activated immune cells and regulate systemic metabolism, we sought inspiration in neoplastic tumor research. This idea is based on the notion that both tumors and activated immune cells share commonthe features of their cellular metabolism because both use Hif1α-triggered aerobic glycolysis as the predominant metabolic program (Biswas and Mantovani 2012; Nagao et al. 2019). They also share the impact on systemic metabolism, as both cancer patients and septic patients exhibit a wasting-like phenotype caused by cytokine-induced insulin resistance (Dev, Bruera, and Dalal 2018). Although insulin resistance is mostly studied as a pathological condition, its evolutionary conservation indicates that it must carry an important physiological function (Soeters and Soeters 2012; Odegaard and Chawla 2013). Hence, we hypothesize that activated immune cells may release the same factors as cancer cells, but with a beneficial role for the acute response as opposed to cancer-induced cachexia.

In this study, we focus on the insulin/IGF antagonist ImpL2 (Imaginal morphogenesis protein-Late 2) as a potential candidate for such a role since it is released by neoplastic cancer cells to suppress insulin signaling via binding to *Drosophila* insulin-like peptides thus causing energy wasting (Alee 2011; Arquier et al. 2006; Honegger et al. 2008; Kwon et al. 2015; Figueroa-Clarevega and Bilder 2015). Besides the production by neoplastic tumors, ImpL2 is known to be released by lipid-overloaded macrophages (Morgantini et al. 2019), as well as other cells employing metabolic programs dependent on the activity of Hif1α in *Drosophila* (Alee 2011; Owusu-Ansah, Song, and Perrimon 2013; Kwon et al. 2015; Figueroa-Clarevega and Bilder 2015). Therefore, we decided to test the role of ImpL2 as a macrophage-derived signaling factor responsible for nutrient mobilization during the acute immune response to bacterial infection.

We show here that activated macrophages produce ImpL2 in the acute phase of infection, resulting in Foxo-mediated changes in adipose tissue metabolism. As an outcome of the ImpL2 action, we observed an increased titer of circulating carbohydrates and lipids as well as their accumulation in macrophages. The role of ImpL2 is necessary for effective resistance to streptococcal infection and effective phagocytosis. In contrast to this beneficial role in the fight against extracellular pathogens, the effects of ImpL2 are maladaptive in response to intracellularly growing *Listeria*, and its chronic activation leads to developmental defects and excessive melanization. Conservation of ImpL2 function between insects and mammals is indicated by increased expression of the ImpL2 homolog IGFBP7 in streptococcus-treated human macrophages.

Results

ImpL2 expression increases in immune-activated macrophages in a Hif1α-dependent manner

93 To test the potential role of ImpL2 during infection, we first monitored its expression profile during
94 the acute phase of *Streptococcus pneumoniae* infection. ImpL2 expression increased significantly in
95 infected flies compared to PBS-injected controls, starting as early as 3 hours post-infection (hpi) and
96 reaching up to a 3-fold increase in expression 21 hpi at the whole organism level (Figure 1A). We
97 employed a transcript-specific ImpL2-RA Gal4 driver (Bader et al. 2013) to drive the fluorescent
98 marker UAS-mCherry to identify tissues responsible for infection-induced rise in ImpL2 expression.
99 The pattern of ImpL2-positive cells resembled the characteristic distribution of macrophages in adult
100 flies (Figure 1B). Moreover, the number of these mCherry-expressing cells increased substantially
101 upon infection (Figure 1B and E). To verify that the cells expressing ImpL2-mCherry are phagocytes,
102 we injected the flies with the phagocytic marker *S. aureus*-pHrodo-Green and it indeed co-localized
103 with these cells (Figure 1C). In addition, cells expressing ImpL2 also actively recognized and engulfed
104 *S. pneumoniae* bacteria *ex vivo* (Figure 1D). The fact that ImpL2 production induced by infection is
105 specific for macrophages is supported by its increased expression in FACS-sorted CrqGal4>UAS-GFP-
106 labeled macrophages (Figure 1F).

107 Since there are three alternative transcriptional start sites for ImpL2, we decided to analyze the
108 expression pattern of each isoform 24 hpi to better understand the regulation of their expression.
109 Consistent with the expression pattern of the *ImpL2-RA* transcript-specific Gal4 driver (Figure 1B),
110 *ImpL2-RA* transcript expression was the highest of all transcript variants in macrophages and was
111 hardly detectable in fat body or muscles (Figure 1G). While the *ImpL2-RB+D* forms were the most
112 abundant variants in adipose tissue, their expression was five-times weaker than *ImpL2-RA* in
113 macrophages (check the different y-axis scales in Figure 1G). In addition, the expression of the *ImpL2-*
114 *RA* isoform increased eightfold in macrophages, indicating the most significant increase in expression
115 compared to other transcripts in response to infection (Figure 1G). The *ImpL2-RA* transcript variant
116 expressed in macrophages is therefore a major contributor to the overall increase in ImpL2
117 expression observed at the onset of infection.

118 The previously characterized metabolic switch of activated macrophages is regulated by the
119 transcriptional factor Hif1α (Krejčová et al. 2019), which is known to be a potent regulator of ImpL2
120 expression in cells relying on anaerobic metabolism (Allee 2011, Li et al. 2013; Owusu-Ansah, Song,
121 and Perrimon 2013). We, therefore, hypothesized that the same regulation could underlie the
122 infection-induced rise in ImpL2 in activated macrophages. Macrophage-specific knockdown of Hif1α
123 during infection (see Figure 1-figure supplement 1A for efficiency) resulted in the inability of these
124 cells to trigger characteristic infection-induced ImpL2 expression, and this effect was particularly
125 evident in the *ImpL2-RA* isoform (Figure 1H). We identified a cluster of four Hif1α binding sites
126 upstream of the macrophage-specific transcription start site of *ImpL2-RA* (Figure 1I). In addition, this
127 enhancer region shows the strongest hypoxic induction of any sequence surrounding the ImpL2 gene
128 (Kamps-Hughes et al. 2015 and Figure 1I), suggesting that Hif1α may directly drive the transcription
129 of ImpL2-RA in macrophages. In-depth analysis of this 500-bp region revealed the presence of eight
130 immune and stress response elements that cluster together (four hypoxia response elements, two
131 Relish bindings sites, and two heat-shock factor binding sites; Figure 1I and Figure 1-figure
132 supplement 2).

133 **These experiments identified activated macrophages as the predominant producers of ImpL2 in**
134 **infected adult flies. The increase of ImpL2 production is associated with the metabolic switch**
135 **induced by Hif1α in macrophages, presumably by direct binding of Hif1α and other stress-related**
136 **transcription factors to the regulatory sequence of the *ImpL2-RA* isoform.**

137

138 **Macrophage-derived ImpL2 is required for mobilization of reserves to be utilized by macrophages**

139 Activated macrophages release signaling factors to mobilize reserves to provide sufficient nutrients
140 for the activated immune system. We show here that macrophages increase ImpL2 production
141 during infection, and because ImpL2 was previously associated with reserve mobilization that led to
142 wasting in flies with cancer, we further tested the impact of macrophage-derived ImpL2 on systemic
143 metabolism.

144 For this purpose, we employed Drosophila genetic tools for either macrophage-specific (CrqGal4) or
145 macrophage-specific and time-restricted (HmlGal4, Gal80^{TS}) manipulation of ImpL2 expression. Using
146 conventional constructs for ImpL2 knockdown (ImpL2^{RNAi}) and overexpression (ImpL2^{CDS}), we
147 achieved significant changes in ImpL2 expression (see Figure 1-figure supplement 1B for efficiency).
148 Such experimental manipulations allowed us, on the one hand, to prevent upregulation of ImpL2 in
149 macrophages induced by infection and, on the other hand, to simulate an increase of ImpL2 in
150 uninfected individuals.

151 Both infection and overexpression of ImpL2 in macrophages significantly reduced triglyceride content
152 in whole flies (Figure 2A), accompanied by dramatic changes in adipose tissue morphology (Figure
153 2B-E). The average size of lipid droplets decreased with increasing number (Figure 2B, C, and E). The
154 overall area of adipose tissue occupied by lipid droplets was markedly smaller (Figure 2D). It should
155 be emphasized that these infection-induced effects were suppressed by macrophage-specific ImpL2
156 knockdown (Figure 2B-E). Detailed lipidomic analysis of adipose tissue by mass spectrometry
157 revealed that both infection and macrophage-specific overexpression of ImpL2 cause a proportional
158 shift of lipid content from storage lipid forms (triglycerides) to polar lipid species
159 (phosphatidylethanolamine, phosphatidylinositol) participating in lipid mobilization and transport
160 (Figure 2F). These effects were hampered by ImpL2 knockdown (Figure 2F). Similar effects were also
161 observed for glycogen stores when both infection and macrophage-specific overexpression of ImpL2
162 significantly reduced glycogen content in whole flies, and knockdown of ImpL2 suppressed this effect
163 (Figure 2G). These data thus indicate that macrophage-derived ImpL2 may serve as a mediator of
164 crosstalk between the immune system and adipose tissue.

165 Besides substantially increased lipolytic and glycogenolytic programs in the adipose tissue of infected
166 individuals, we also observed enhanced autophagy in the adipose tissue of Atg8a-mCherry-bearing
167 flies (Figure 3A), further implying an increase in catabolic metabolism. These metabolic changes
168 induced by infection are consistent with the expression pattern of many metabolic genes in adipose
169 tissue. The *MTP*, *apoLPP*, *apoLTP,* and *Bmm* genes associated with lipid mobilization, as well as the
170 autophagy-associated *Atg1* and *Atg6* genes, all increased in adipose tissue during infection (Figure 3B
171 and Figure 3-figure supplement 1) and were under the control of macrophage-derived ImpL2.
172 Indeed, ImpL2 knockdown suppressed this effect, while ImpL2 overexpression mimicked the
173 infection-induced response (Figure 3B and Figure 3-figure supplement 1). A remarkable number of
174 these genes are known to be Foxo targets. The transcriptional activity of Foxo is regulated by insulin
175 signaling and because ImpL2 is an antagonist of insulin signaling, we analyzed the impact of
176 macrophage-derived ImpL2 on the subcellular localization of Foxo in adipose tissue. We found that
177 Foxo was clearly localized to the nucleus upon infection, while remaining mostly in the cytoplasm of
178 adipocytes of uninfected flies (Figure 4). Macrophage-specific overexpression of ImpL2 recapitulated
179 the infection-induced pattern and, conversely, knockdown reversed the effect of infection on Foxo
180 localization (Figure 4); these effects of ImpL2 on Foxo localization are in agreement with the
181 expression of Foxo target genes (Figure 3B and Figure 3-figure supplement 1).

182 Stimulated catabolism of glycogen and triglycerides is manifested by hyperglycemia and
183 hyperlipidemia in the circulation of infected flies when increased titers of glucose, trehalose, and
184 cholesteryl-ester were detected in their hemolymph (Figure 5A-D). Accordingly, infection-activated
185 macrophages increased the accumulation of these energy-rich compounds and cholesterol as a
186 cholesteryl-ester derivative (Figure 5E-H). These results are supported by the increased occurrence of

lipid droplets in the cytosol of macrophages activated by infection and stained with the neutral lipid dye OilRedO (Figure 5I and J). The ability of activated macrophages to recognize and uptake lipoproteins was verified by injection of labeled human lipoproteins (LDL-pHrodo; Figure 5K) that can be endocytosed by the activity of the scavenger receptor croquemort (fly homolog of CD36), which is abundantly expressed in *Drosophila* macrophages. The mobilization of reserves, which leads to an increase in the amount of nutrients in the circulation and subsequently to their increased uptake by macrophages, depends on the production of ImpL2 by macrophages. Indeed, macrophage-specific ImpL2 knockdown suppresses all observed effects stimulated by infection, while ImpL2 overexpression mimics these effects even in uninfected individuals (Figure 5A-I).

Combining all these results, we can conclude that ImpL2, produced by macrophages during infection, triggers a Foxo-mediated transcriptional program in adipose tissue that provides macrophages with the necessary nutrients.

ImpL2 is required for an effective immune response but can be detrimental during chronic infection

The efficiency of the immune response depends on the supply of sufficient energy and the necessary precursors to the activated immune cells. Therefore, we decided to investigate whether the ImpL2-mediated metabolic supplementation for macrophages is essential for mounting an adequate immune response. The lack of ImpL2 produced by macrophages significantly reduced the survival of *S. pneumoniae*-infected flies (Figure 6A), which was reflected in the elevated pathogen load (Figure 6B), both indicating a decreased resistance in these individuals. This notion was further supported by the reduced phagocytic rate in these flies (Figure 6E and F). Interestingly, overexpression of ImpL2 24 hours prior to infection improved the resistance of these individuals to streptococcal infection, as evidenced by lower pathogen load and improved survival (Figure 6C and D). These observations suggest that ImpL2, produced by metabolically activated acute phase macrophages, is essential for systemic metabolic changes that support their efficient bactericidal function.

Although our results demonstrate a beneficial role of ImpL2 during acute infection, previous work showing the pathological role of ImpL2 in cancer-induced cachexia (Kwon et al. 2015) suggests that the beneficial role of ImpL2 may be restricted to a short-time window of acute response. Therefore, we tested the effects of ImpL2 overexpression in macrophages over the lifespan of developing individuals and also challenged flies with chronic infection caused by the intracellular pathogen *Listeria monocytogenes*. Interestingly, the mere transient overexpression of ImpL2 in macrophages led to a frequent occurrence of melanized spots (Figure 7A); even more severe outcomes were achieved by overexpression of ImpL2 during development, resulting in a smaller adult size (data not shown; similar result to Honegger et al. 2008) accompanied by impaired dorsal closure in roughly half of the individuals (Figure 7A). In addition, overexpression of ImpL2 reduced resistance to *L. monocytogenes* infection with chronically increased pathogen burden (Figure 7D and E), suggesting that the enhanced effects of ImpL2, in contrast to the acute response, are detrimental in chronic infection. Consistent with this result, suppression of ImpL2 production improved survival and significantly reduced bacterial load during this chronic type of infection (Figure 7B and C).

In conclusion, ImpL2-mediated reallocation of resources to macrophages is essential for an adequate antibacterial immune response and resistance to infection. On the other hand, chronic or excessive production of ImpL2 can cause developmental defects and rather enhance the deleterious effects of chronic infections.

Gene expression of *ImpL2* mammalian homolog *IGFBP7* is increased in immune-activated THP-1 cells

234 We have previously shown that IGFBP7, the mammalian homologue of ImpL2, is produced by lipid-
235 loaded liver macrophages in response to feeding a high fat diet, with consequent effects on systemic
236 metabolism through the regulation of insulin signaling in hepatocytes. Notably, ImpL2 released from
237 lipid-loaded macrophages appears to play an analogous role in obese *Drosophila* (Morgantini et al.
238 2019). To test the relevance of the role of ImpL2 in humans during infection, we measured the
239 expression of IGFBPs in PMA-activated THP-1 human monocytic cell line 24 hours after exposure to *S.*
240 *pneumoniae* bacteria (Figure 8A). The expression of *IGFBP1*, *IGFBP2*, *IGFBP5,* and *IGFBP6* was not
241 detected, indicating that these genes are not expressed in these cells (data not shown). Interestingly,
242 *IGFBP7* gene expression was significantly increased in inoculated culture compared to PBS-treated
243 controls (Figure 8B). In addition, gene expression of anti-inflammatory *IGFBP3* was reduced four-fold
244 while *IGFBP4* showed no significant change (Figure 8B). **These data therefore indicate that the**
245 **increase in ImpL2 / IGFBP7 production by macrophages in response to infection is evolutionarily**
246 **conserved in mammals. These results not only validate the importance of the acute bacterial**
247 **infection model in *Drosophila* but also suggest that investigating the role of IGFBP7 in systemic**
248 **metabolic regulation and inter-organ communication during infection would be of interest in**
249 **humans.**

250

251 **Discussion**

252 In this work, we show that infection-driven Hif1α transcriptional activity connects intracellular
253 metabolic switch with ImpL2 production in activated macrophages. ImpL2 subsequently induces the
254 mobilization of adipose tissue resources to be provided for activated immune cells. This metabolic
255 rearrangement of adipose tissue is mediated by the transcription factor Foxo, which results in the
256 acceleration of lipolysis and assembly of lipoproteins. The increased titer of circulating lipids
257 facilitates the utilization of lipids by macrophages and thus supports their bactericidal function
258 (Figure 9). Although such ImpL2-induced metabolic adaptation is essential for an acute immune
259 response, it can become maladaptive in cases of its chronic activation or infection by intracellular
260 pathogens that metabolically exploit the host cell. This can be considered a remarkable example of
261 how a beneficial metabolic program can become maladaptive in chronic diseases. That this
262 mechanism might not be limited to insects is indicated by an experiment showing that human
263 macrophages activated by the same bacteria increase the expression of IGFBP7, the human homolog
264 of *Drosophila* ImpL2.

265

266 We have previously shown that *Drosophila* macrophages undergo evolutionarily conserved
267 polarization to the M1 phenotype, thus adjusting their metabolism toward Hif1α-induced aerobic
268 glycolysis in response to bacterial challenge. This cellular metabolic shift is accompanied by systemic
269 metabolic changes necessary to supplement the sudden needs of macrophages (Krejčová et al.
270 2019). Coordination of cellular metabolism in macrophages with systemic metabolism is crucial for
271 resistance to infection and anticipates the existence of circulating factors mediating this inter-organ
272 crosstalk (Dolezal et al. 2019). Inspired by research on neoplastic cancer cells (Kwon et al. 2015;
273 Figueroa-Clarevega and Bilder 2015; Bunker et al. 2015), we focus in this study on the cachectic
274 factor ImpL2 as a candidate previously linked to Hif1α transcriptional activity while having the
275 potential to regulate systemic metabolism (Alee 2011; Li et al. 2013). To test whether the
276 interconnection between Hif1α activity and ImpL2 expression during hypoxia also applies to
277 infection-activated macrophages, we performed a genomic *in silico* meta-analysis of hypoxic
278 enhancer activity and Hif1α binding sites (Kamps-Hughes et al. 2015). This approach revealed the
279 induction of a hypoxic enhancer in close vicinity to the transcription start site of the *ImpL2-RA*
280 transcript variant, which is further supported by the presence of four hypoxia response elements at
281 this locus. *ImpL2-RA* is the most strongly expressed transcriptional variant in macrophages and its
282 expression increases even more after infection. **This infection-induced increase depends on Hif1α,**

indicating a connection of ImpL2 expression with an internal metabolic switch in infection-activated macrophages.

We have previously identified extracellular adenosine as an immune cell-derived systemic factor with an analogous function to ImpL2 in mobilizing carbohydrate stores to be available to the immune system (Bajgar et al. 2015; Bajgar and Dolezal 2018). In addition to regulating carbohydrate metabolism, a prominent effect of ImpL2 is the regulation of systemic lipid metabolism. As documented in this work by various approaches, **macrophage-derived ImpL2 mediates infection-induced catabolic processes in adipose tissue resulting in the assembly and release of lipoproteins for the redistribution of resources to metabolically demanding tissues. Thus, infection-induced ImpL2 production results in an increased titer of circulating lipids, which are then used by macrophages to effectively fight invading pathogens.** The observed metabolic changes in infection-challenged flies resemble lipemia as a characteristic symptom of sepsis in severely ill patients (Harris, Gosnell, and Kumwenda 2000). In sepsis-induced lipemia, hepatocytes release low-density lipoproteins (LDL) and very low-density lipoproteins (VLDL), providing lipids to be preferentially utilized by bactericidal macrophages in the periphery (Khovidhunkit et al. 2004; Aspichueta et al. 2012). Scavenger receptor-mediated endocytosis of serum lipoproteins, together with attenuated reverse cholesterol transport, both contribute substantially to cholesterol accumulation in bactericidal immune cells (Podrez et al. 2000). There are many immune-related functions in macrophages dependent on sufficient delivery of lipids, from phagocytosis and maturation of phagolysosome to catecholamine production or immune memory formation via the mevalonate pathway (summarized in Remmerie and Scott 2018). Although providing substantial amounts of lipids to macrophages is essential for their proper function during the acute phase of infection, chronic exposure of macrophages to excessive lipids may lead to the adoption of a foam-cell phenotype promoting metabolic syndrome and atherosclerosis (Chistiakov et al. 2017; Febbraio, Guy, and Silverstein 2004).

Although the mechanism of infection-induced lipid catabolism and lipoprotein assembly has not been fully elucidated, we revealed that nuclear translocation of Foxo, followed by increased expression of several Foxo-target genes involved in this process, was regulated by macrophage-derived ImpL2. Since Foxo-driven mobilization of lipid stores requires suppression of insulin signaling in adipose tissue (Molaei, Vandehoef, and Karpac 2019; Luong et al. 2006), the effect of ImpL2 can be explained by its well-documented ability to bind *Drosophila* insulin-like peptides (DILPs) and thus reduce insulin sensitivity in adipose tissue (Alee 2011; Alic et al. 2011; Arquier et al. 2006; Figueroa-Clarevega and Bilder 2015; Honegger et al. 2008; Kwon et al. 2015; Okamoto et al. 2013). Metabolic adjustments and the switch from anabolism to catabolism in adipose tissue during infection is regulated by multiple mechanisms (reviewed in Dolezal et al. 2019). In particular, Foxo has previously been associated with wasting in flies with chronic infection (Dionne et al. 2006), indicating rather its pathological effects during the prolonged immune response. Based on the aforementioned, the simplest explanation for the effect of ImpL2 on the mobilization of adipose tissue sources is the suppression of insulin signaling to allow a metabolic program triggered by Foxo. **The remote ImpL2 effect on reserve mobilization described in this work therefore represents a beneficial role of ImpL2 during the acute immune response**. Suppression of insulin signaling is often associated with chronic inflammation and may become harmful to the organism by disrupting the metabolic balance. However, the theoretical concept of selfish immunity (Straub 2014) sees insulin resistance as an evolutionary adaptive mechanism for rerouting nutrients toward immunity during the acute immune response. Our results showing that ImpL2 is required for an effective immune response through changes in lipid metabolism can be considered as experimental evidence of insulin resistance as an adaptive mechanism for mobilization of sources for acute phase of immune response.

Neoplastic tumors share a characteristic cellular metabolism (Warburg 1925) with bactericidal macrophages (Andrejeva and Rathmell 2017). **Here, we show that they may also share the production of ImpL2, originally perceived as a cancer-derived cachectic factor** (Kwon et al. 2015;

333 Figueroa-Clarevega and Bilder 2015), **to regulate systemic metabolism.** Both tumor cells and
334 activated immune cells produce ImpL2 and thus subsequently silence systemic insulin signaling as a
335 result of the adoption of Hif1α-triggered aerobic glycolysis. The perception of ImpL2 expression as a
336 consequence of the cellular metabolic state is further supported by other conditions of
337 mitochondria-independent generation of ATP, such as experimentally induced mitochondrial
338 dysfunction, hypoxia, and neoplastic tumor growth (Alee 2011; Figueroa-Clarevega and Bilder 2015;
339 Kwon et al. 2015; Li et al. 2013). Although this mechanism is beneficial to the organism in acute
340 infection, it becomes harmful in the case of tumor growth or chronic infection, as demonstrated here
341 by the negative effect of ImpL2 on survival during chronic infection caused by the intracellular
342 pathogen *L. monocytogenes*. This can be explained by the known behavior of various intracellular
343 bacteria that use the supply of host cells and hijack their metabolic cascades to literarily nourish
344 themselves (Péan et al. 2017; Teng, Ang, and Guan 2017).

345 Our results revealed that human macrophages, activated by *S. pneumoniae*, increase the expression
346 of IGFBP7, the human homolog of Drosophila ImpL2, suggesting that a similar mechanism may
347 function in humans. Notably, not only infection but also experimentally induced metabolic syndrome
348 in both *Drosophila* and mammals led to increased expression of ImpL2/IGFBP7 in macrophages
349 (Morgantini et al. 2019). While ImpL2-producing macrophages affect metabolism in the *Drosophila*
350 fat body (integrating functions of both mammalian adipose tissue and liver), IGFBP7-producing
351 Kupffer cells act directly on hepatocytes in order to induce systemic metabolic changes (Morgantini
352 et al. 2019; Akiel et al. 2017). The ability of both ImpL2 and IGFBP7 to bind extracellular insulin,
353 thereby reducing systemic insulin signaling, further documents their functional homology, suggesting
354 that the mechanism of their action may also be conserved (Honegger et al. 2008; Arquier et al. 2006;
355 Oh et al. 1996). Accordingly, LPS-administered Kupffer cells have been shown to produce cytokines to
356 affect Foxo-mediated release of LDL and VLDL from hepatocytes (Kamagate et al. 2008; Sparks and
357 Dong 2009; Aspichueta et al. 2012). Although this mechanism of resource mobilization may be
358 important for the acute phase response, when prolonged, it contributes to the progression of
359 metabolic syndrome and atherosclerosis (Tomkin 2012). It is therefore not surprising that the levels
360 of circulating IGFBP7 are considered a marker of systemic metabolic imbalances accompanying
361 several human diseases, such as obesity, acute kidney injury, liver fibrosis, and chronic obstructive
362 pulmonary disease (Liu et al. 2015; Gunnerson et al. 2016; Martínez-Castillo et al. 2020; Ruan et al.
363 2017).

364 Taking our data together with previous work, we can conclude that the insulin/IGF antagonist ImpL2,
365 released from M1 macrophages as a reflection of their metabolic polarization, mediates the
366 mobilization of nutrients from adipose tissue by inducing insulin resistance to provide sufficient
367 resources for the immune system. Despite the fact that both ImpL2 and insulin resistance are mostly
368 studied in the context of pathological conditions such as cancer-induced cachexia, obesity and
369 chronic inflammatory conditions, our data revealed that they may play a beneficial role in the acute
370 phase of bacterial infection. In addition, the relevance of our model is supported by the production
371 of IGFBP7, the ImpL2 homolog, in response to streptococcal infection in human macrophages. This
372 leads us to the hypothesis that analogous mechanisms may also apply to macrophage-induced
373 nutrient mobilization from hepatocytes during the acute phase of the immune response, which may
374 become detrimental under chronic conditions.

375

376 **Funding**

377 Tomáš Doležal - Czech Science Foundation (Project 20-09103S)

378 Adam Bajgar - Czech Science Foundation (Project 20-14030S)

379 Gabriela Krejčová - USB Grant Agency (Project 050/2019/P)

Acknowledgment

The authors acknowledge funding from the Grant Agency of the Czech Republic to TD (Project 20-09103S; www.gacr.cz) and to AB (Project 20-14030S; www.gacr.cz). GK was supported by USB Grant Agency (Project 050/2019/P). We thank to Lucie Hrádková for laboratory services, enthusiasm and support, Alena Krejčí-Bruce and Lenka Chodáková for critical comments and inspiring discussions, Pavel Branný and Linda Doubravová for help with the preparation of the S.p.-GFP strain and Hana Sehadová for help with scanning electron microscopy. We thank to Hugo Stocker for the ImpL2^{RNAi}, ImpL2^{CDS}, and ImpL2-RA-Gal4 fly lines, Gabor Juhasz for the Atg8amCherry fly, and Marc Dionne for Crq>GFP fly line. Other fly stocks were obtained from the Bloomington Center (Bloomington, IN) and the VDRC (Vienna, Austria). The *S. pneumoniae* and *L. monocytogenes* bacterial strains were obtained from Dr. David Schneider. We also thank Martin Moss and Petr Šimek for the lipidomics service, the Department of Medical Biology (USB) for allowing us to use the S3eBioRad sorter, Biology Centre CAS for allowing us to use a confocal microscope, and a laboratory equipped to maintain human tissue cultures. We are also grateful to developers of Fiji: an open-source platform for biological-image analysis (doi:10.1038/nmeth.2019)

MATERIALS AND METHODS

Drosophila melanogaster strains

The flies were raised on a diet containing cornmeal (80 g/l), sucrose (50 g/l), yeast (40 g/l), agar (10 g/l), and 10%-methylparaben (16.7 mL/l) and maintained in a humidity-controlled environment with a natural 12 h/12 h light/dark cycle at 25˚C. Flies carrying Gal80 protein were raised at 18˚C and transferred to 29˚C 24 h prior to infection in order to degrade temperature-sensitive Gal80. Prior to the experiments, flies were kept in plastic vials on a sucrose-free cornmeal diet (cornmeal 53.5 g/l, yeast 28.2 g/l, agar 6.2 g/l and 10%-methylparaben 16.7 mL/l) for 7 days. Flies infected with *S. pneumoniae* were kept on a sucrose-free cornmeal diet in incubators at 29˚C due to the temperature sensitivity of *S. pneumoniae*. They were transferred to fresh vials every other day without the use of CO_2 to ensure good food condition. Flies infected with *L. monocytogenes* were kept on a sucrose-free cornmeal diet at 25˚C. The Drosophila Stock Center in Bloomington provided *ImpL2^{RNAi}* (*y1 sc* v1; P{TRiP.HMC03863}attP40*; FBst0055855) *TRiP^{control}* (*y[1] v[1] ; P{y[+t7.7]=CaryP}attP40*; FBst0036304) and *20xUAS-6xmCherry* (*P{20XUAS-6XmCherry-HA}attP2*; FBtp0094992) flies. *ImpL2-Gal4* (*ImpL2-RA-Gal4*; FBal0290965) and *UAS-ImpL2^{cds}* (*UAS-s.ImpL2*; FBal0249386) were kind gifts from Hugo Stocker. *CrqGal4>2xeGFP* were obtained from Marc Dionne. The *Atg8a-mCherry* strain was kindly provided by Gabor Juhasz. The *w^{1118}* strain has a genetic background based on *CantonS*.

Genotypes of experimental models

Figure 1

ImpL2Gal4>UASmCherry corresponds to *+/+; 20xUAS-6xmCherry/+; ImpL2-Gal4/+*

HmlGal4>GFP refers to *HmlΔ-Gal4 UAS-2xeGFP/HmlΔ-Gal4 UAS-2xeGFP; +/+*

HmlGal4>GFP; Hif1α^{RNAi} corresponds to *HmlΔ-Gal4 UAS-2xeGFP/UAS-Hif1α^{RNAi}; +/+*

421 **Figure 2**

422 **ImpL2^{RNAi}** refers to *+/+; HmlΔ-Gal4/ UAS-ImpL2^{RNAi}; P{tubPGal80ts}/+*

423 **ImpL2^{cds}** corresponds to *+/+; HmlΔ-Gal4/+; P{tubPGal80ts}/UAS-ImpL2^{cds}*

424 **TRiP^{control}** refers to *+/+; HmlΔ-Gal4/+; P{tubPGal80ts}/TRiP^{control}*

425 **W^{1118}** corresponds to *w^{1118}/+; HmlΔ-Gal4/+; P{tubPGal80ts}/+*

426

427 **Figure 3**

428 **ImpL2^{RNAi}** refers to *+/+; HmlΔ-Gal4/ UAS-ImpL2^{RNAi}; P{tubPGal80ts}/+*

429 **ImpL2^{cds}** corresponds to *+/+; HmlΔ-Gal4/+; P{tubPGal80ts}/UAS-ImpL2^{cds}*

430 **TRiP^{control}** refers to *+/+; HmlΔ-Gal4/+; P{tubPGal80ts}/TRiP^{control}*

431 **W^{1118}** corresponds to *w^{1118}/+; HmlΔ-Gal4/+; P{tubPGal80ts}/+*

432 **Atg8a-mCherry** refers to gen *+/+; Atg8a-mCherry/Atg8a-mCherry*

433

434 **Figure 4**

435 **ImpL2^{RNAi}** refers to *+/+; HmlΔ-Gal4/ UAS-ImpL2^{RNAi}; P{tubPGal80ts}/+*

436 **ImpL2^{cds}** corresponds to *+/+; HmlΔ-Gal4/+; P{tubPGal80ts}/UAS-ImpL2^{cds}*

437 **TRiP^{control}** refers to *+/+; HmlΔ-Gal4/+; P{tubPGal80ts}/TRiP^{control}*

438 **W^{1118}** corresponds to *w^{1118}/+; HmlΔ-Gal4/+; P{tubPGal80ts}/+*

439

440 **Figure 5**

441 **ImpL2^{RNAi}** refers to *+/+; HmlΔ-Gal4/ UAS-ImpL2^{RNAi}; P{tubPGal80ts}/+*

442 **ImpL2^{cds}** corresponds to *+/+; HmlΔ-Gal4/+; P{tubPGal80ts}/UAS-ImpL2^{cds}*

443 **TRiP^{control}** refers to *+/+; HmlΔ-Gal4/+; P{tubPGal80ts}/TRiP^{control}*

444 **W^{1118}** corresponds to *w^{1118}/+; HmlΔ-Gal4/+; P{tubPGal80ts}/+*

445 **Crq>Gal4; UAS2xGFP x ImpL2^{RNAi}** refers to *+/+; UAS-ImpL2^{RNAi}/+; Crq-Gal4, UAS-2xeGFP/+*

446 **Crq>Gal4; UAS2xGFP x ImpL2^{cds}** corresponds to *+/+; +/+; Crq-Gal4, UAS-2xeGFP/UAS-ImpL2^{cds}*

447 **Crq>Gal4; UAS2xGFP x TRiP^{control}** refers to *+/+; +/+; Crq-Gal4, UAS-2xeGFP/TRiP^{control}*

448 **Crq>Gal4; UAS2xGFP x W^{1118}** corresponds to *w^{1118}/+; Crq-Gal4, UAS-2xeGFP/+*

449 **CrqGal4>GFP** refers to *+/+; Crq-Gal4, UAS-2xeGFP/Crq-Gal4, UAS-2xeGFP*

450

451 **Figure 6**

452 **ImpL2^{RNAi}** refers to *+/+; HmlΔ-Gal4/ UAS-ImpL2^{RNAi}; P{tubPGal80ts}/+*

453 **ImpL2^{cds}** corresponds to *+/+; HmlΔ-Gal4/+; P{tubPGal80ts}/UAS-ImpL2^{cds}*

454 **TRiP^{control}** refers to *+/+; HmlΔ-Gal4/+; P{tubPGal80ts}/TRiP^{control}*

455 **W^{1118}** corresponds to *w^{1118}/+; HmlΔ-Gal4/+; P{tubPGal80ts}/+*

456 **Crq>Gal4; UAS2xGFP x ImpL2^{RNAi}** refers to *+/+; UAS-ImpL2^{RNAi}/+; Crq-Gal4, UAS-2xeGFP/+*

457 **Crq>Gal4; UAS2xGFP x ImpL2^{cds}** corresponds to *+/+; +/+; Crq-Gal4, UAS-2xeGFP/UAS-ImpL2^{cds}*

458 **Crq>Gal4; UAS2xGFP x TRiP^{control}** refers to *+/+; +/+; Crq-Gal4, UAS-2xeGFP/TRiP^{control}*

459 **Crq>Gal4; UAS2xGFP x W^{1118}** corresponds to *w^{1118}/+; Crq-Gal4, UAS-2xeGFP/+*

460 **CrqGal4>GFP** refers to *+/+; Crq-Gal4, UAS-2xeGFP/Crq-Gal4, UAS-2xeGFP*

461

462 **Figure 7**

463 **ImpL2^{RNAi}** refers to *+/+; HmlΔ-Gal4/ UAS-ImpL2^{RNAi}; P{tubPGal80ts}/+*

464 **ImpL2^{cds}** corresponds to *+/+; HmlΔ-Gal4/+; P{tubPGal80ts}/UAS-ImpL2^{cds}*

465 **TRiP^{control}** refers to *+/+; HmlΔ-Gal4/+; P{tubPGal80ts}/TRiP^{control}*

466 **W^{1118}** corresponds to *w^{1118}/+; HmlΔ-Gal4/+; P{tubPGal80ts}/+*

467 **Crq>Gal4 x ImpL2^{cds}** corresponds to *+/+; +/+; Crq-Gal4, UAS-2xeGFP/UAS-ImpL2^{cds}*

468

469 **Hypoxic enhancer activity analysis**

470 Genome-wide experimental data characterizing hypoxia-induced transcriptional enhancer activity
471 (Kamps-Hughes et al. 2015) was used to analyze the ImpL2 region for hypoxic enhancers. Hypoxic
472 transcriptional induction is defined as the ratio of expressed randomer tag counts in hypoxic versus
473 normoxic conditions and was binned by 500-bp regions across the *ImpL2* locus. Each 500-bp bin was
474 then analyzed for transcription factor binding sites corresponding to hypoxic (Hif1α), immune (Rel)
475 and stress (HSF) response transcription factors. Transcription factor position frequency matrices
476 were downloaded from the JASPAR database
477 (https://academic.oup.com/nar/article/32/suppl_1/D91/2505159) and queried against the 500-bp
478 bin sequences using BOBRO software (https://www.ncbi.nlm.nih.gov/pmc/articles/PMC3074163/).
479 BOBRO generates a p-value of enrichment for the position frequency matrix within the search
480 sequence and also identifies the location of the predicted binding sites.

481 **Gene expression analysis**

482 Gene expression analyzes were performed on several types of samples: six whole flies, six thoraxes,
483 six fat bodies, or 20,000 isolated macrophages. Macrophages were isolated by a cell sorter as
484 described in (Krejčová et al. 2019) while dissections were made in PBS, transferred to TRIzol Reagent
485 (Invitrogen) and homogenized using a DEPC-treated pestle. Subsequently, RNA was extracted by
486 TRIzol Reagent (Invitrogen) according to the manufacturer's protocol. Superscript III Reverse
487 Transcriptase (Invitrogen) primed by oligo(dT)20 primer was used for reverse transcription. Relative
488 expression rates for particular genes were quantified on a 384CFX 1000 Touch Real-Time Cycler (Bio-

489 Rad) using the TP 2x SYBR Master Mix (Top-Bio) in three technical replicates with the following
490 protocol: initial denaturation - 3 min at 95˚C, amplification – 15 s at 94˚C, 20 s at 56˚C, 25 s at 72˚C
491 for 40 cycles. Melting curve analysis was performed at 65–85˚C/step 0.5˚C. The primer sequences are
492 listed in the Key Resources Table. The qPCR data were analyzed using double delta Ct analysis, and
493 the expressions or specific genes were normalized to the expression of Ribosomal protein 49 (Rp49)
494 in the corresponding sample. The relative values (fold change) to control are shown in the graphs.
495 Samples for gene expression analysis were collected from three independent experiments. Data
496 were compared with ANOVA followed by Tukey's multiple comparisons test in Graphpad Prism
497 software. Sidak's multiple comparison correction was performed.

498 **Metabolite measurement**

499 To measure metabolite concentration, isolated macrophages, whole flies or hemolymph were used.
500 Macrophages were isolated from 25 adult males by centrifugation (14,000 RPM, 5 min) through a
501 silicagel filter into 50 µL of PBS. For measurement of metabolites from whole flies, five flies were
502 homogenized in 200 µL of PBS and centrifuged (3 min, 4˚C, 8,000 RPM) to discard insoluble debris.
503 50,000 macrophages were isolated by cell sorter as described above. Half of all samples were used
504 for the quantification of proteins. Samples for glucose, glycogen, trehalose, and triglyceride
505 measurement were denatured at 75˚C for 10 min, whereas samples for protein quantification were
506 frozen immediately in -80˚C. Glucose was measured using a Glucose (GO) Assay (GAGO-20) Kit
507 (Sigma) according to the manufacturer's protocol. Colorimetric reaction was measured at 540 nm.
508 For glycogen quantification, sample was mixed with amyloglucosidase (Sigma) and incubated at 37˚C
509 for 30 min. A Bicinchoninic Acid Assay (BCA) Kit (Sigma) was used for protein quantification according
510 to the supplier's protocol and the absorbance was measured at 595 nm. Cholesterol and cholesteryl
511 esters were measured on isolated lipid fraction by using Cholesterol/Cholesteryl Ester Quantitation
512 Kit (Sigma) according to the supplier´s protocol. Triglycerides were measured using Triglyceride
513 quantification Colorimetric/Fluorometric Kit (Sigma). For trehalose quantification, sample was mixed
514 with trehalase (Sigma) and incubated at 37˚C for 30 min. Samples for metabolite concentration were
515 collected from three independent experiments. Measured data were compared in Graphpad Prism
516 using ANOVA followed by Tukey's multiple comparisons test. Sidak's multiple comparison correction
517 was performed.

518 **Staining of lipid droplets**

519 Flies were dissected in Grace´s Insect Medium (Sigma) and subsequently stained with DAPI and Cell
520 Brite Fix Membrane Stain 488 (Biotium) diluted with Grace´s Insect Medium according to the
521 manufacturer´s protocol at 37˚C. Tissues were washed in PBS and then fixed with 4% PFA
522 (Polysciences). After 20 min, the tissues were washed in PBS and pre-washed with 60% isopropanol.
523 Dissected abdomens were then stained with OilRedO dissolved in 60% isopropanol for 10 min. The
524 tissues were then washed with 60% isopropanol and mounted in an Aqua Polymount (Polysciences).
525 Tissues were imaged using an Olympus FluoView 3000 confocal microscope (Olympus). Content of
526 lipids in adipose tissue and size of lipid droplets were analyzed using Fiji software. Flies for the
527 analysis of LDs in the fat body were collected from three independent experiments and
528 representative images are shown.

529 **Lipidomic analysis**

530 Adipose tissues from six flies from each group were dissected in ice-cold PBS for lipidomics analysis.
531 The removed tissues were stored in PBS buffer in Eppendorf tubes at – 80 °C. Immediately after
532 thawing, they were extracted by 500 µl of cold chloroform: methanol solution (v/v; 1:1). The samples
533 were then homogenized by a Tissue Lyser II (Qiagen, Prague, Czech Republic) at 50 Hz, -18°C for 5

534 min and kept further in an ultrasonic bath (0°C, 5 min). Further, the mixture was centrifuged at
535 10,000 RPM at 4°C for 10 min followed by the removal of the supernatant. The extraction step was
536 repeated at the same conditions. The lower layer of pooled supernatant was evaporated to dryness
537 under a gentle stream of Argon. The dry total lipid extract was re-dissolved in 500 µl of chloroform:
538 methanol solution (v/v; 1:1) and directly measured using previously described methods (Bayley et al.
539 2020). Briefly, high performance liquid chromatography (Accela 600 pump, Accela AS autosampler)
540 combined with mass spectrometry LTQ-XL (all Thermo Fisher Scientific, San Jose, CA, USA) were used.
541 The chromatographic conditions were as follows: Injection volume 5 µl; column Gemini 3 µM C18
542 HPLC column (150 × 2 mm ID, Phenomenex, Torrance, CA, USA) at 35°C; the mobile phase (A) 5 mM
543 ammonium acetate in methanol with ammonia (0.025%), (B) water and (C) isopropanol: MeOH (8:2);
544 gradient change of A:B:C as follows: 0 min: 92:8:0, 7 min: 97:3:0, 12 min: 100:0:0, 19 min: 93:0:7, 20-
545 29 min: 90:0:10, 40-45 min: 40:0:60, 48 min: 100:0:0, and 50-65 min: 92:8:0 with flow rate 200
546 µl/min. The mass spectrometry condition: positive (3 kV) and negative (-2,5 kV) ion detection mode;
547 capillary temperature 200°C. Eluted ions were detected with full scan mode from 200 to 1000 Da
548 with the collisionally induced MS2 fragmentation (NCE 35). Data were acquired and processed by
549 means of XCalibur 4.0 software (Thermo Fisher). The corrected areas under individual analytical
550 peaks were expressed in percentages assuming that the total area of all detected is 100%.

551 **Autophagy visualization**

552 To visualize autophagy in adipose tissue, Atg8a-mCHerry-bearing flies were dissected in PBS, fixed
553 with 4% PFA, and then washed with PBS and stained with DAPI. Fat bodies were imaged using an
554 Olympus FluoView 3000 confocal microscope (Olympus).

555 **Foxo subcellular localization**

556 Adipose tissues for immunolocalization of Foxo were dissected in ice-cold PBS. Dissection was
557 followed by 20-min fixation in 4% PFA in PBS. After three washing steps in PBS-Tween (0.1%),
558 unspecific binding was blocked with 10% NGS in PBS for 1 h at RT. The tissues were then incubated
559 with primary antibody diluted in ratio 1:1,000 (Rabbit Drosophila anti-Foxo, CosmoBio) at 4°C
560 overnight. After washing the unbound primary antibody (three times for 10 min in PBST), the
561 secondary antibody was applied in dilution 1:250 for 2 h at RT (Cy2 Goat anti-Rabbit, Jackson-
562 Immunoresearch). The nuclei were stained with DAPI. Tissues were mounted with Aqua-Polymount
563 (Polysciences), DAPI was used for nuclear staining. Foxo localization was detected by Plot-Profile
564 analysis in FIJI.

565 **Isolation of macrophages**

566 GFP-labeled macrophages were isolated from *Crq-Gal4, UAS-eGFP* male flies using fluorescence-
567 activated cell sorting (FACS). Approximately 200 flies were anaesthetized with CO_2, washed in PBS
568 and homogenized in 600 mL of PBS using a pestle. The homogenate was sieved through a nylon cell
569 strainer (40 µm). This strainer was then additionally washed with 200 µL of PBS, which was added to
570 the homogenate subsequently. The samples were centrifuged (3 min, 4˚C, 3,500 RPM) and the
571 supernatant was washed with ice-cold PBS after each centrifugation (three times). Prior to sorting,
572 samples were transferred to FACS polystyrene tubes using a disposable bacterial filter (50 µm,
573 Sysmex) and macrophages were sorted into 100 µL of PBS using a S3™ Cell Sorter (BioRad). Isolated
574 cells were verified by fluorescence microscopy and differential interference contrast.

575 **Phagocytic activity**

576 To visualize phagocytic activity, flies were injected with 50 nl of pHrodo™ Green *S. aureus* (Thermo
577 Fischer Scientific) using an Eppendorf Femtojet microinjector. After 1 h, the flies were fixed in 4% PFA
578 for 45 min, washed in PBS and subsequently mounted on imaging dishes using an Aqua Polymount
579 (Polysciences). Thoraxes were imaged using an Olympus FluoView 3000 confocal microscope. To
580 analyze phagocytic rate, flies were infected with 20,000 of *S. pneumoniae* and after 24 h, they were
581 injected with 50 nl of pHrodo™ Red *S. aureus* (Thermo Fischer Scientific). After 1 h, abdomens of flies
582 were opened in PBS and the macrophages were allowed to attach to a microscopic imaging dish for
583 40 min. Subsequently, the PBS was removed and the cells were fixed for 20 min with 4% PFA. Aqua
584 Polymount (Polysciences) was used to mount the sample. Macrophages were imaged using an
585 Olympus FluoView 3000 confocal microscope and red dots depicting phagocytic events were
586 manually counted per cell.

587 **Lipoprotein uptake**

588 To document the uptake of lipoproteins by *Drosophila* macrophages, flies were injected with 50 nl of
589 pHrodo™ Red LDL (Thermo Fischer Scientific) using an Eppendorf Femtojet microinjector. After 1 h,
590 abdomens of flies were opened in PBS and the macrophages were allowed to attach to a microscopic
591 imaging dish for 40 min. Subsequently, the PBS was removed and cells were fixed for 20 min with 4%
592 PFA. Aqua Polymount (Polysciences) was used to mount the sample. Macrophages were imaged
593 using an Olympus FluoView 3000 confocal microscope.

594 **Bacterial strain and fly injection**

595 The *Streptococcus pneumoniae* strain EJ1 was stored at -80˚C in Tryptic Soy Broth (TSB) media
596 containing 10% glycerol. For the experiments, bacteria were streaked onto agar plates containing 3%
597 TSB and 100 mg/mL streptomycin and subsequently incubated at 37˚C in 5% CO_2 overnight. Single
598 colonies were inoculated into 3 mL of TSB liquid media with 100 mg/mL of streptomycin and 100,000
599 units of catalase and incubated at 37˚C + 5% CO2 overnight. Bacterial density was measured after an
600 additional 4 h so that it reached an approximate 0.4 OD600. Final bacterial cultures were centrifuged
601 and dissolved in PBS so the final OD reached 2.4. The *S. pneumoniae* culture was kept on ice prior to
602 injection and during the injection itself. Seven-day-old males were anaesthetized with CO_2 and
603 injected with 50 nL culture containing 20,000 *S. pneumoniae* bacteria or 50 nL of mock buffer (PBS)
604 into the ventrolateral side of the abdomen using an Eppendorf Femtojet microinjector. The *Listeria*
605 *monocytogenes* strain 10403S was stored at -80°C in brain and heart infusion (BHI) broth containing
606 25% glycerol. For the experiments bacteria were streaked onto Luria Bertani (LB) agar plates
607 containing 100 µg/mL streptomycin and incubated at 37°C overnight; plates were stored at 4°C and
608 used for inoculation for a period of two weeks. Single colonies were used to inoculate 3 mL of BHI
609 and incubated overnight at 37°C without shaking to obtain a morning 600 nm optical density (OD600)
610 of approx. 0.4. Further, *L. monocytogenes* cultures were diluted to OD600 0.01 in phosphate
611 buffered saline (PBS) and stored on ice prior to loading into an injection needle. Approximately 1,000
612 *Listeria* per fly were injected.

613 **Survival analysis**

614 *Streptococcus*-injected flies were kept at 29˚C in vials with approximately 30 individuals per vial and
615 were transferred to fresh food every other day. *Listeria*-injected flies were kept at 25˚C. Dead flies
616 were counted daily. At least three independent experiments were performed and combined into a
617 single survival curve generated in Graphpad Prism software; individual experiments showed
618 comparable results. The average number of individuals was more than 500 for each genotype and
619 replicate. Data were analyzed by Log-rank and Grehan-Breslow Wilcoxon tests (which gave more
620 weight to deaths at early time points).

621 **Pathogen load measurement**

622 Single flies were homogenized in PBS using a motorized plastic pestle in 1.5 mL tubes. Bacteria were
623 plated in spots onto LB (*L. monocytogenes*) or TSB (*S. pneumoniae*) agar plates containing
624 streptomycin in serial dilutions and incubated overnight at 37°C before manual counting. To
625 determine intracellular *L. monocytogenes* loads, flies were injected with 50 nL of gentamycin solution
626 (1 mg/mL in PBS) 3 h prior to fly homogenization. Pathogen loads of 16 flies were determined for
627 each genotype and treatment in each experiment; at least three independent infection experiments
628 were conducted and the results were combined into one graph (in all presented cases, individual
629 experiments showed comparable results).

630 **THP-1 cell lines**

631 THP-1 cells were cultured at 37°C, 5% CO2, in RPMI-1640 medium (Sigma), supplemented with 2 mM
632 glutamine (Applichem), 2 g/L sodium bicarbonate (J&K Scientific), 10% FBS (Biosera) and 100 mg/L
633 streptomycin (Sigma). Prior to the experiment, cells were transferred to 24-well plates at 10^5
634 cells/well in four biological replicates. THP-1 cells were activated with phorbol-12-myristate-13-
635 acetate (200 ng/mL, MedChemExpress). After 24 hours, *S. pneumoniae* bacteria were added (MOI 50
636 bacteria/macrophage) and the plate was centrifuged briefly (2 min, 200xg). Following 6-h incubation,
637 the cells were washed with RPMI-1640 medium, and fresh RPMI-1640 supplemented with
638 gentamycin (0.1 mg/mL, Sigma) was added. After 1 h incubation, the medium was replaced with
639 RPMI-1640 supplemented with penicillin-streptomycin (1%, Biosera). After amother 17 h, the cells
640 were harvested into TRIzol Reagent (Invitrogen) followed by RNA isolation.
641

642

643 **Key resources table**

644

Reagent type (species) or resource	Designation	Source reference	Identifier	Additional information
Strain, strain background (*Streptococcus pneumoniae*)	*EJ1* strain	Provided by David Schneider		Dilution 20,000 units
Chemical compound, drug	TRIzol Reagent	Invitrogen	Cat# 15-596-018	
Chemical compound, drug	Superscript III Reverseerse Transcriptase	Invitrogen	Cat# 18080044	
Chemical compound, drug	2x SYBR Master Mix	Top-Bio	Cat# T607	

Reagent type (species) or resource	Designation	Source reference	Identifier	Additional information
Chemical compound, drug	Grace´s Insect Medium	Sigma	Cat# G9771-1L	
Chemical compound, drug	Oil Red O	Sigma	Cat# O0625-25G	
Chemical compound, drug	DAPI	Sigma	Cat# D9542	
Chemical compound, drug	Cell Brite Fix Membrane Stain 488	Biotium	Cat# 30090-T	
Chemical compound, drug	Phalloidin blue	ThermoFisher	Cat# A30104	
Chemical compound, drug	pHrodo™ Red S. aureus Bioparticles™ Conjugate for Phagocytosis	ThermoFisher	Cat# A10010	
Chemical compound, drug	Phorbol-12-myristate-13-acetate	MedChemExpress	Cat# HY-18739	
Chemical compound, drug	RPMI-1640 Medium	Sigma	Cat# R7755	
Chemical compound, drug	Glutamine	Applichem	Cat# A3704	
Chemical compound, drug	Gentamycin	Sigma	Cat# 1405-41-0	
Chemical compound, drug	FBS	Biosera	Cat# FB-1001	
Chemical	Penicilin-Streptomycin	Biosera	Cat#	

Reagent type (species) or resource	Designation	Source reference	Identifier	Additional information
compound, drug			XC-A4122/100	
Chemical compound, drug	Protease inhibitor mixture	Sigma	Cat# SRE0055	
Chemical compound, drug	Phosphatase inhibitor	Thermo-Fisher	Cat# A32957	
Antibody	anti-Akt	Cell Signaling Technology	Cat# 9272	
Antibody	anti-phospho Ser505-Akt	Cell Signaling Technology	Cat# 4054	
Antibody	Alpha-Catenin	Development Studies Hybridoma Bank	Cat# DCAT-1	
Chemical compound, drug	SuperSignal ECL substrate	Thermo-Fisher	Cat# 34075	
Antibody	Rabbit Drosophila anti-Foxo	CosmoBio	Cat# THU-A-DFoxo	
Antibody	Cy2 Goat anti-Rabbit	Jackson-Immunoresearch	AB_2338021	
Commercial assay, kit	Glucose (GO) Assay Kit	Sigma	Cat# GAGO20-1KT	
Commercial assay, kit	Bicinchoninic Acid Assay Kit	Sigma	Cat# BCA1	
Commercial assay, kit	Cholesterol/Cholesteryl Ester Quantitation Kit	Sigma	Cat# 428901-1KIT	
Commercial assay, kit	Triglyceride quantification Colorimetric/Fluorometric Kit	Sigma	Cat# MAK266-	

Reagent type (species) or resource	Designation	Source reference	Identifier	Additional information
			1KT	
Chemical compound, drug	Trehalase from porcine kidney	Sigma	Cat# T8778-1UN	
Genetic reagent (*Drosophila melanogaster*)	*HmlG4G80: w*; HmlΔ-Gal4*; P{tubPGal80ts}**	Cross made in our laboratory by Tomas Dolezal		
Genetic reagent (*Drosophila melanogaster*)	ImpL2^{RNAi}	Bloomington Drosophila Stock Center		
Genetic reagent (*Drosophila melanogaster*)	ImpL2 Gal4	Provided by Hugo Stocker		
Genetic reagent (*Drosophila melanogaster*)	Atg8a-mCherry	Provided by Gabor Juhasz		
Genetic reagent (*Drosophila melanogaster*)	ImpL2^{cds}	Provided by Hugo Stocker		
Genetic reagent (*Drosophila melanogaster*)	20xUAS-6xmCherry	Bloomington Drosophila Stock Center		
Genetic reagent (*Drosophila melanogaster*)	CrqGal4>2xeGFP	Provided by Marc C. Dionne		
Genetic reagent (*D. melanogaster)*	*Hif1α[RNAi]: P{KK110834}VIE-260B*	Vienna Drosophila Resource Center	VDRC: v106504	FBst0478328
Genetic reagent (*D. melanogaster*)	*TRiP^{control}: y(1) v(1); P{y[+t7.7]=CaryP}attP2*	Bloomington Drosophila Stock Center	BDSC: 36303	FBst0036303
Genetic reagent (*D. melanogaster)*	*w: w^{1118}*	Genetic background based on CantonS		

Reagent type (species) or resource	Designation	Source reference	Identifier	Additional information
Sequence-based reagent	Foxo forward: CAATGCAAGAGATGGTCTCTC	KRD	CG3143	FBgn0038197
Sequence-based reagent	Foxo reverse: TGACCAGGTTCGTGTTGACC	KRD	CG3143	FBgn0038197
Sequence-based reagent	4EBP Forward: CCATGATCACCAGGAAGGTTGTCA	KRD	CG8846	FBgn0261560
Sequence-based reagent	4EBP Reverse: AGCCCGCTCGTAGATAAGTTTGGT	KRD	CG8846	FBgn0261560
Sequence-based reagent	EIF-4E Forward: AAGAAGAACATTCGCCCATG T	KRD	CG4035	FBgn0015218
Sequence-based reagent	EIF-4E Reverse: GGACTGCCGACGGAAACAAC	KRD	CG4035	FBgn0015218
Sequence-based reagent	Glut-CoA deh Forward: CTGATTGGTGCCTTTGGCC	KRD	CG9547	FBgn0031824
Sequence-based reagent	Glut-CoA deh Reverse: ATAGCGAGCGTTGTTCAGAC	KRD	CG9547	FBgn0031824
Sequence-based reagent	Lip4 Forward: CCACTTGGGTGATGATGGGAC	KRD	CG6113	FBgn0032264
Sequence-based reagent	Lip4 Reverse: ACGTATTGCCACGAACATTGG	KRD	CG6113	FBgn0032264
Sequence-based reagent	MTP Forward: GAATCGAAATGCCCAGACG	KRD	CG9342	FBgn0266369
Sequence-based reagent	MTP Reverse: AACGTTGGTTTGTTTGAGAAGC	KRD	CG9342	FBgn0266369
Sequence-based reagent	HSL Forward: CAGTCCTACGAGATTCACGG	KRD	CG11055	FBgn0034491
Sequence-based reagent	HSL Reverse: GGCTTCGTTGGATAACATTGTG	KRD	CG11055	FBgn0034491
Sequence-based	Bmm Forward: CACCGCGCCGCAATGAATGTATA	KRD	CG5295	FBgn0036449

Reagent type (species) or resource	Designation	Source reference	Identifier	Additional information
reagent	A			
Sequence-based reagent	Bmm Reverse: TTCAATCACTGTTTGTCGGTCGGC	KRD	CG5295	FBgn0036449
Sequence-based reagent	GlyP Forward: TCCACCCTGAGGGACTACTAC	KRD	CG7254	FBgn0004507
Sequence-based reagent	GlyP Reverse: GGTGTTGGTCAGTGAGCGAC	KRD	CG7254	FBgn0004507
Sequence-based reagent	GlyS Forward: CGATGAAGAAGTACAGGGTC	KRD	CG6904	FBgn0266064
Sequence-based reagent	GlyS Reverse: TATCATCGTTATTGCCTGGAG	KRD	CG6904	FBgn0266064
Sequence-based reagent	apoLTP Forward: TGGGTGGATTGAAGCCACAG	KRD	CG15828	FBgn0032136
Sequence-based reagent	apoLTP Reverse: TGAGTGGATTTTCTCTCACTGC	KRD	CG15828	FBgn0032136
Sequence-based reagent	apoLPP Forward: TTGGAATCCTAGCTTCTGTGCT	KRD	CG11064	FBgn0087002
Sequence-based reagent	apoLPP Reverse: AGTCATAGTAGTTGCCGGGTAT	KRD	CG11064	FBgn0087002
Sequence-based reagent	Atg1 Forward: CTAAAGCCGTCGTCCAATGT	KRD	CG10967	FBgn0260945
Sequence-based reagent	Atg1 Reverse: GAACAGCATGCTCCGGTATT	KRD	CG10967	FBgn0260945
Sequence-based reagent	Atg6 Forward: CGGAGTTATCTTTGCCCATCT	KRD	CG5429	FBgn0264325
Sequence-based reagent	Atg6 Reverse: GTGCTACACGCTGTTGCTC	KRD	CG5429	FBgn0264325
Sequence-based reagent	Rp49 Forward: AAGCTGTCGCACAAATGGCG	KRD	CG7939	FBgn0002626

Reagent type (species) or resource	Designation	Source reference	Identifier	Additional information
Sequence-based reagent	Rp49 Reverse: GCACGTTGTGCACCAGGAAC	KRD	CG7939	FBgn0002626
Sequence-based reagent	ImpL2 Forward: TTCGCGGTTTCTGGGCACCC	KRD	CG15009	FBgn0001257
Sequence-based reagent	ImpL2 Reverse: GCGCGTCCGATCGTCGCATA	KRD	CG15009	FBgn0001257
Sequence-based reagent	ImpL2-RA Forward: GTGCCAACGAAGCTTCGAGTG	KRD	CG15009	FBgn0001257
Sequence-based reagent	ImpL2-RA Reverse: GCGTGGCTTCTCCTCCTCC	KRD	CG15009	FBgn0001257
Sequence-based reagent	ImpL2-RB, D Forward: GTCGTCGGAAAGGATACCGC	KRD	CG15009	FBgn0001257
Sequence-based reagent	ImpL2-RB, D Reverse: TTCCGTCGTCAATCCAATAGCC	KRD	CG15009	FBgn0001257
Sequence-based reagent	ImpL2-RC Forward: ATAGACTCGGAGACCTCCCC	KRD	CG15009	FBgn0001257
Sequence-based reagent	ImpL2-RC Reverse: GCGTGGCTTCTCCTCCTCC	KRD	CG15009	FBgn0001257
Sequence-based reagent	IGFBP7 Forward: GCCATCACCCAGGTCAGCAAG	KRD	GC04M057030	
Sequence-based reagent	IGFBP7 Reverse: GGATTCCGATGACCTCACAGCT	KRD	GC04M057030	
Sequence-based reagent	ACTB Forward: ATTGCCGACAGGATGCAGAA	KRD	GC07M005527	
Sequence-based reagent	ACTB Reverse: GCTGATCCACATCTGCTGGAA	KRD	GC07M005527	

Reagent type (species) or resource	Designation	Source reference	Identifier	Additional information
Sequence-based reagent	IGFBP1 Forward: TCCTTTGGGACGCCATCAGTAC	KRD	GC07P046 552	
Sequence-based reagent	IGFBP1 Reverse: GATGTCTCCTGTGCCTTGGCTA	KRD	GC07P046 552	
Sequence-based reagent	IGFBP2 Forward: CGAGGGCACTTGTGAGAAGCG	KRD	GC02P216 632	
Sequence-based reagent	IGFBP2 Reverse: TGTTCATGGTGCTGTCCACGTG	KRD	GC02P216 632	
Sequence-based reagent	IGFBP3 Forward: CGCTACAAAGTTGACTACGAGTC	KRD	GC07M045 912	
Sequence-based reagent	IGFBP3 Reverse: GTCTTCCATTTCTCTACGGCAGG	KRD	GC07M045 912	
Sequence-based reagent	IGFBP4 Forward: ACCCACGAGGACCTCTACATCA	KRD	GC17P040 443	
Sequence-based reagent	IGFBP4 Reverse: CACACCAGCACTTGCCACGCT	KRD	GC17P040 443	
Sequence-based reagent	IGFBP5 Forward: CGTGCTGTGTACCTGCCCAATT	KRD	GC02M216 672	
Sequence-based reagent	IGFBP5 Reverse: ACTTGTCCACGCACCAGCAGAT	KRD	GC02M216 672	
Sequence-based reagent	IGFBP6 Forward: CACAGGATGTGAACCGCAGAGA	KRD	GC12P053 097	
Sequence-based reagent	IGFBP6 Reverse: CACTGAGTCCAGATGTCTACGG	KRD	GC12P053 097	
Software, algorithm	Graphpad Prism	https://www.graphpad.com/	Graphpad Prism	RRID:SCR_002798

Reagent type (species) or resource	Designation	Source reference	Identifier	Additional information
Software, algorithm	Microsoft Excel	https://www.microsoft.com/	Microsoft Excel	
Software, algorithm	Fiji	ImageJ - https://fiji.sc	ImageJ	RRID:SCR_002285
Other	S3e Cell Sorter	BioRad -http://www.bio-rad.com/	BioRad	
Other	Olympus FluoView 3000	Olympus - https://www.olympus-global.com/	Olympus	RRID:SCR_017015 RRID:SCR_014215
Other	Olympus IX71	Olympus - https://www.olympus-global.com/	Olympus	

647 **References**

648 Alee. 2011. "ImpL2 Represses Insulin Signaling in Response to Hypoxia." Dissertation Thesis.
649 University of Oregon, Eugene, Oregon, USA.

650 Akiel, Maaged et al. 2017. "IGFBP7 Deletion Promotes Hepatocellular Carcinoma." *Cancer Research*
651 77(15): 4014–25. http://cancerres.aacrjournals.org/lookup/doi/10.1158/0008-5472.CAN-16-
652 2885.

653 Alic, Nazif, Matthew P. Hoddinott, Giovanna Vinti, and Linda Partridge. 2011. "Lifespan Extension by
654 Increased Expression of the Drosophila Homologue of the IGFBP7 Tumour Suppressor." *Aging*
655 *Cell* 10(1): 137–47. http://doi.wiley.com/10.1111/j.1474-9726.2010.00653.x.

656 Andrejeva, Gabriela, and Jeffrey C. Rathmell. 2017. "Similarities and Distinctions of Cancer and
657 Immune Metabolism in Inflammation and Tumors." *Cell Metabolism* 26(1): 49–70.
658 https://linkinghub.elsevier.com/retrieve/pii/S1550413117303467.

659 Arquier, Nathalie et al. 2006. "Analysis of the Hypoxia-Sensing Pathway in Drosophila Melanogaster."
660 *Biochemical Journal* 393(2): 471–80.
661 https://portlandpress.com/biochemj/article/393/2/471/78893/Analysis-of-the-hypoxiasensing-
662 pathway-in.

663 Aspichueta, Patricia et al. 2012. "Disrupted VLDL Features and Lipoprotein Metabolism in Sepsis." In
664 *Dyslipidemia - From Prevention to Treatment*, InTech.
665 http://www.intechopen.com/books/dyslipidemia-from-prevention-to-treatment/disrupted-
666 vldl-features-and-lipoprotein-metabolism-in-sepsis.

667 Bader, R. et al. 2013. "The IGFBP7 Homolog Imp-L2 Promotes Insulin Signaling in Distinct Neurons of
668 the Drosophila Brain." *Journal of Cell Science* 126(12): 2571–76.
669 http://jcs.biologists.org/cgi/doi/10.1242/jcs.120261.

670 Bajgar, Adam et al. 2015. "Extracellular Adenosine Mediates a Systemic Metabolic Switch during
671 Immune Response" ed. Marc S. Dionne. *PLOS Biology* 13(4): e1002135.
672 https://dx.plos.org/10.1371/journal.pbio.1002135.

673 Bajgar, Adam, and Tomas Dolezal. 2018. "Extracellular Adenosine Modulates Host-Pathogen
674 Interactions through Regulation of Systemic Metabolism during Immune Response in
675 Drosophila" ed. Brian P. Lazzaro. *PLOS Pathogens* 14(4): e1007022.
676 https://dx.plos.org/10.1371/journal.ppat.1007022.

677 Bayley, Jeppe Seamus et al. 2020. "Cold-Acclimation Increases Depolarization Resistance and
678 Tolerance in Muscle Fibers from a Chill-Susceptible Insect, Locusta Migratoria." *American*
679 *Journal of Physiology-Regulatory, Integrative and Comparative Physiology*: ajpregu.00068.2020.
680 https://journals.physiology.org/doi/10.1152/ajpregu.00068.2020.

681 Biswas, Subhra K., and Alberto Mantovani. 2012. "Orchestration of Metabolism by Macrophages."
682 *Cell Metabolism* 15(4): 432–37.
683 https://linkinghub.elsevier.com/retrieve/pii/S1550413112000150.

684 Van den Bossche, Jan, Luke A. O'Neill, and Deepthi Menon. 2017. "Macrophage Immunometabolism:
685 Where Are We (Going)?" *Trends in Immunology* 38(6): 395–406.
686 https://linkinghub.elsevier.com/retrieve/pii/S147149061730042X.

687 Bunker, Brandon D et al. 2015. "The Transcriptional Response to Tumorigenic Polarity Loss in
688 Drosophila." *eLife* 4. http://www.ncbi.nlm.nih.gov/pubmed/25719210.

689 Chistiakov, Dimitry A. et al. 2017. "Mechanisms of Foam Cell Formation in Atherosclerosis." *Journal*

690 *of Molecular Medicine* 95(11): 1153–65. http://link.springer.com/10.1007/s00109-017-1575-8.

691 Dev, R, E. Bruera, and S. Dalal. 2018. "Insulin Resistance and Body Composition in Cancer Patients."
692 *Annals of Oncology* 29: ii18-ii26.
693 https://linkinghub.elsevier.com/retrieve/pii/S0923753419316801.

694 Dionne, Marc S., Linh N. Pham, Mimi Shirasu-Hiza, and David S. Schneider. 2006. "Akt and Foxo
695 Dysregulation Contribute to Infection-Induced Wasting in Drosophila." *Current Biology* 16(20):
696 1977–85. https://linkinghub.elsevier.com/retrieve/pii/S0960982206020641.

697 Dolezal, Tomas et al. 2019. "Molecular Regulations of Metabolism during Immune Response in
698 Insects." *Insect Biochemistry and Molecular Biology* 109: 31–42.
699 https://linkinghub.elsevier.com/retrieve/pii/S0965174818304600.

700 Febbraio, Maria, Ella Guy, and Roy L. Silverstein. 2004. "Stem Cell Transplantation Reveals That
701 Absence of Macrophage CD36 Is Protective Against Atherosclerosis." *Arteriosclerosis,*
702 *Thrombosis, and Vascular Biology* 24(12): 2333–38.
703 https://www.ahajournals.org/doi/10.1161/01.ATV.0000148007.06370.68.

704 Figueroa-Clarevega, Alejandra, and David Bilder. 2015. "Malignant Drosophila Tumors Interrupt
705 Insulin Signaling to Induce Cachexia-like Wasting." *Developmental Cell* 33(1): 47–55.
706 https://linkinghub.elsevier.com/retrieve/pii/S1534580715001434.

707 Gunnerson, Kyle J. et al. 2016. "TIMP2•IGFBP7 Biomarker Panel Accurately Predicts Acute Kidney
708 Injury in High-Risk Surgical Patients." *Journal of Trauma and Acute Care Surgery* 80(2): 243–49.
709 http://journals.lww.com/01586154-201602000-00009.

710 H. Tomkin, Gerald. 2012. "LDL as a Cause of Atherosclerosis." *The Open Atherosclerosis & Thrombosis*
711 *Journal* 5(1): 13–21. http://benthamopen.com/ABSTRACT/TOATHERTJ-5-13.

712 Harris, H W, J E Gosnell, and Z L Kumwenda. 2000. "The Lipemia of Sepsis: Triglyceride-Rich
713 Lipoproteins as Agents of Innate Immunity." *Journal of endotoxin research* 6(6): 421–30.
714 http://www.ncbi.nlm.nih.gov/pubmed/11521066.

715 Honegger, Basil et al. 2008. "Imp-L2, a Putative Homolog of Vertebrate IGF-Binding Protein 7,
716 Counteracts Insulin Signaling in Drosophila and Is Essential for Starvation Resistance." *Journal of*
717 *Biology* 7(3): 10. http://jbiol.biomedcentral.com/articles/10.1186/jbiol72.

718 Kamagate, Adama et al. 2008. "FoxO1 Mediates Insulin-Dependent Regulation of Hepatic VLDL
719 Production in Mice." *Journal of Clinical Investigation*. http://www.jci.org/articles/view/32914.

720 Kamps-Hughes, Nick, Jessica L. Preston, Melissa A. Randel, and Eric A. Johnson. 2015. "Genome-Wide
721 Identification of Hypoxia-Induced Enhancer Regions." *PeerJ* 3: e1527.
722 https://peerj.com/articles/1527.

723 Kelly, Beth, and Luke AJ O'Neill. 2015. "Metabolic Reprogramming in Macrophages and Dendritic
724 Cells in Innate Immunity." *Cell Research* 25(7): 771–84.
725 http://www.nature.com/articles/cr201568.

726 Khovidhunkit, Weerapan et al. 2004. "Thematic Review Series: The Pathogenesis of Atherosclerosis.
727 Effects of Infection and Inflammation on Lipid and Lipoprotein Metabolism Mechanisms and
728 Consequences to the Host." *Journal of Lipid Research* 45(7): 1169–96.
729 http://www.jlr.org/lookup/doi/10.1194/jlr.R300019-JLR200.

730 Krejčová, Gabriela et al. 2019. "Drosophila Macrophages Switch to Aerobic Glycolysis to Mount
731 Effective Antibacterial Defense." *eLife* 8. https://elifesciences.org/articles/50414.

732 Kwon, Young et al. 2015. "Systemic Organ Wasting Induced by Localized Expression of the Secreted

733 Insulin/IGF Antagonist ImpL2." *Developmental Cell* 33(1): 36–46.
734 https://linkinghub.elsevier.com/retrieve/pii/S1534580715001148.

735 Li, Yan et al. 2013. "HIF- and Non-HIF-Regulated Hypoxic Responses Require the Estrogen-Related
736 Receptor in Drosophila Melanogaster" ed. Eric Rulifson. *PLoS Genetics* 9(1): e1003230.
737 https://dx.plos.org/10.1371/journal.pgen.1003230.

738 Liu, Yi et al. 2015. "Serum IGFBP7 Levels Associate with Insulin Resistance and the Risk of Metabolic
739 Syndrome in a Chinese Population." *Scientific Reports* 5(1): 10227.
740 http://www.nature.com/articles/srep10227.

741 Luong, Nancy et al. 2006. "Activated FOXO-Mediated Insulin Resistance Is Blocked by Reduction of
742 TOR Activity." *Cell Metabolism* 4(2): 133–42.
743 https://linkinghub.elsevier.com/retrieve/pii/S1550413106002348.

744 Martínez-Castillo, Moisés et al. 2020. "Differential Production of Insulin-like Growth Factor-Binding
745 Proteins in Liver Fibrosis Progression." *Molecular and Cellular Biochemistry* 469(1–2): 65–75.
746 http://link.springer.com/10.1007/s11010-020-03728-4.

747 Molaei, Maral, Crissie Vandehoef, and Jason Karpac. 2019. "NF-KB Shapes Metabolic Adaptation by
748 Attenuating Foxo-Mediated Lipolysis in Drosophila." *Developmental Cell* 49(5): 802–810.e6.
749 https://linkinghub.elsevier.com/retrieve/pii/S1534580719302795.

750 Morgantini, Cecilia et al. 2019. "Liver Macrophages Regulate Systemic Metabolism through Non-
751 Inflammatory Factors." *Nature Metabolism* 1(4): 445–59.
752 http://www.nature.com/articles/s42255-019-0044-9.

753 Nagao, Ayako et al. 2019. "HIF-1-Dependent Reprogramming of Glucose Metabolic Pathway of
754 Cancer Cells and Its Therapeutic Significance." *International Journal of Molecular Sciences* 20(2):
755 238. https://www.mdpi.com/1422-0067/20/2/238.

756 Newsholme, P, R Curi, S Gordon, and E A Newsholme. 1986. "Metabolism of Glucose, Glutamine,
757 Long-Chain Fatty Acids and Ketone Bodies by Murine Macrophages." *Biochemical Journal*
758 239(1): 121–25. https://portlandpress.com/biochemj/article/239/1/121/21648/Metabolism-of-
759 glucose-glutamine-longchain-fatty.

760 Nicholson, David, and Lindsay B. Nicholson. 2008. "A Simple Immune System Simulation Reveals
761 Optimal Movement and Cell Density Parameters for Successful Target Clearance." *Immunology*
762 123(4): 519–27. http://doi.wiley.com/10.1111/j.1365-2567.2007.02721.x.

763 Odegaard, J. I., and A. Chawla. 2013. "Pleiotropic Actions of Insulin Resistance and Inflammation in
764 Metabolic Homeostasis." *Science* 339(6116): 172–77.
765 https://www.sciencemag.org/lookup/doi/10.1126/science.1230721.

766 Oh, Youngman et al. 1996. "Synthesis and Characterization of Insulin-like Growth Factor-Binding
767 Protein (IGFBP)-7." *Journal of Biological Chemistry* 271(48): 30322–25.
768 http://www.jbc.org/lookup/doi/10.1074/jbc.271.48.30322.

769 Okamoto, N. et al. 2013. "A Secreted Decoy of InR Antagonizes Insulin/IGF Signaling to Restrict Body
770 Growth in Drosophila." *Genes & Development* 27(1): 87–97.
771 http://genesdev.cshlp.org/cgi/doi/10.1101/gad.204479.112.

772 Owusu-Ansah, Edward, Wei Song, and Norbert Perrimon. 2013. "Muscle Mitohormesis Promotes
773 Longevity via Systemic Repression of Insulin Signaling." *Cell* 155(3): 699–712.
774 https://linkinghub.elsevier.com/retrieve/pii/S0092867413011586.

775 Péan, Claire B. et al. 2017. "Regulation of Phagocyte Triglyceride by a STAT-ATG2 Pathway Controls

776 Mycobacterial Infection." *Nature Communications* 8(1): 14642.
777 http://www.nature.com/articles/ncomms14642.

778 Podrez, Eugene A. et al. 2000. "Macrophage Scavenger Receptor CD36 Is the Major Receptor for LDL
779 Modified by Monocyte-Generated Reactive Nitrogen Species." *Journal of Clinical Investigation*
780 105(8): 1095–1108. http://www.jci.org/articles/view/8574.

781 Remmerie, Anneleen, and Charlotte L. Scott. 2018. "Macrophages and Lipid Metabolism." *Cellular*
782 *Immunology* 330: 27–42. https://linkinghub.elsevier.com/retrieve/pii/S0008874918300327.

783 Ruan, Wenjing et al. 2017. "Serum Levels of IGFBP7 Are Elevated during Acute Exacerbation in COPD
784 Patients." *International Journal of Chronic Obstructive Pulmonary Disease* Volume 12: 1775–80.
785 https://www.dovepress.com/serum-levels-of-igfbp7-are-elevated-during-acute-exacerbation-
786 in-copd--peer-reviewed-article-COPD.

787 Shattuck-Heidorn, Heather et al. 2016. "Energetics and the Immune System: Trade-Offs Associated
788 with Non-Acute Levels of CRP in Adolescent Gambian Girls." *Evolution, Medicine, and Public*
789 *Health*: eow034. https://academic.oup.com/emph/article-lookup/doi/10.1093/emph/eow034.

790 Soeters, Maarten R., and Peter B. Soeters. 2012. "The Evolutionary Benefit of Insulin Resistance."
791 *Clinical Nutrition* 31(6): 1002–7.
792 https://linkinghub.elsevier.com/retrieve/pii/S0261561412001112.

793 Sparks, Janet D, and Henry H Dong. 2009. "FoxO1 and Hepatic Lipid Metabolism." *Current Opinion in*
794 *Lipidology* 20(3): 217–26. http://journals.lww.com/00041433-200906000-00012.

795 Straub, Rainer H. 2014. "Insulin Resistance, Selfish Brain, and Selfish Immune System: An
796 Evolutionarily Positively Selected Program Used in Chronic Inflammatory Diseases." *Arthritis*
797 *Research & Therapy* 16(Suppl 2): S4. http://arthritis-
798 research.biomedcentral.com/articles/10.1186/ar4688.

799 Teng, Ooiean, Candice Ke En Ang, and Xue Li Guan. 2017. "Macrophage–Bacteria Interactions—A
800 Lipid-Centric Relationship." *Frontiers in Immunology* 8.
801 http://journal.frontiersin.org/article/10.3389/fimmu.2017.01836/full.

802 Warburg, Otto. 1925. "Über Den Stoffwechsel Der Carcinomzelle." *Klinische Wochenschrift* 4(12):
803 534–36. http://link.springer.com/10.1007/BF01726151.

804 Zmora, Niv, Stavros Bashiardes, Maayan Levy, and Eran Elinav. 2017. "The Role of the Immune
805 System in Metabolic Health and Disease." *Cell Metabolism* 25(3): 506–21.
806 https://linkinghub.elsevier.com/retrieve/pii/S1550413117300967.

807

808

809 **Figure legends**

810

811 Figure 1. **Streptococcal infection increases ImpL2 expression in a Hif1α-dependent manner in**
812 **activated macrophages**

813 (**A**) Expression of ImpL2 mRNA at whole-body level in flies (Crq>GFP) infected with *S. pneumoniae*
814 (Sp. Infection) and control flies (Buff. Injection) at 0, 3, 6, 9, 12, 15, 18 and 21 hpi. (**B**) Representative
815 confocal microscopy images of control (left) and infected (right) ImpL2Gal4>UASmCherry individuals
816 imaged at 24 hpi, from Z stack of 7 layers, autofluorescence in the green channel was used to
817 visualize the fly's body. (**C**) Confocal microscopy images of ImpL2Gal4>UASmCherry hemocyte
818 depicting its phagocytic ability visualized by *S. aureus*-pHrodo-green. The scale bar represents 10 µm.
819 (**D**) Confocal microscopy image of ImpL2Gal4>UASmCherry hemocyte actively interacting with GFP-
820 labeled *S. pneumoniae* (Sp-GFP) *ex vivo.* The scale bar represents 13 µm. (**E**) Number of ImpL2-
821 positive macrophages in the thorax of control and infected adult flies (ImpL2Gal4>UASmCherry) at
822 24hpi. (**F**) Expression of ImpL2 mRNA (using primers targeting all transcript variants) in hemocytes
823 isolated from control and infected Crq>GFP flies at 24hpi. (**G**) Gene expression of ImpL2-RA (left),
824 ImpL2-RB and ImpL2-RD (middle) and ImpL2-RC (right) transcript variants in either hemocytes, fat
825 body or thorax muscles dissected from control and infected Crq>GFP flies at 24 hpi. (**H**) Gene
826 expression of ImpL2 (using primers targeting all transcript variants) and ImpL2-RA in hemocytes
827 isolated from control and infected Crq>GFP flies with and without hemocyte-specific Hif1α
828 knockdown at 24 hpi. (**I**) (I) In silico analysis of hypoxic enhancer activity by 500 bp bins at the ImpL2
829 locus and visualization of ImpL2 transcript variants (Flybase.org). Each black dot plots a log2 fold
830 change (y-axis) of the difference in the randomer tag counts mapped to the 500-bp bin between
831 normoxic and hypoxic conditions. The triangles show the position and negative log10 p-value (y-axis)
832 of multiple hypoxic (Hif1α), immune (Rel) and stress (HSF) response transcription factor binding sites.
833 The close up shows distribution and clustering of individual response elements for the most
834 significant bin. In (**A, F, H**), expression levels normalized against rp49 are reported as fold change
835 relative to levels of ImpL2 (using primers targeting all transcript variants) in PBS-injected Crq>GFP
836 controls, which were arbitrarily set to 1. In (**G**), expression levels normalized against rp49 are
837 reported as fold change relative to levels of ImpL2-RA in hemocytes of PBS-injected Crq>GFP controls
838 for all three graphs. The individual dots represent biological replicates. Values are mean ± SD,
839 asterisks mark statistically significant differences (*p<0.05; **p<0.01; ***p<0.001). Hif1α, hypoxia-
840 inducible factor 1 α; Rel, relish; HSF, heat shock factor.

841

842 Figure 1-figure supplement 1. **Efficiency of genetic manipulations of Hif1α and ImpL2 in *Drosophila***
843 **macrophages**

844 (**A**) Gene expression of Hif1α in hemocytes of Buff-injected flies and *S. pneumoniae*-infected flies
845 with or without macrophage-specific Hif1α knockdown. (**B**) ImpL2 gene expression measured at the
846 whole organism level in flies with macrophage-specific knockdown and overexpression of ImpL2 and
847 their respective controls, either with ImpL2 constructs only or with Gal4 drivers only. Expression
848 levels normalized against rp49 are presented as a fold change relative to levels of ImpL2 in *w;*
849 *ImpL2*^{RNAi} control and Hif1α in uninfected *Hml>Gal4, UAS-GFP x TRiP*^{control}, respectively,
850 which were arbitrarily set to 1. Individual dots represent biological replicates. Values are mean ± SD,
851 asterisks mark statistically significant differences (*p<0.05; **p<0.01; ***p<0.001).

852

853 Figure 1-figure supplement 2. **ImpL2-RA regulatory sequence with transcription factor binding sites**

854 500-bp long sequence upstream of ImpL2-RA transcriptional start site (as shown on map) with
855 marked binding sites for Hif1α, Rel and HSF1. Hif1α, hypoxia-inducible factor 1 α; Rel, relish; HSF1,
856 heat shock factor 1.

857

858 Figure 2. **Macrophage-derived ImpL2 regulates changes in adipose tissue metabolism induced by**
859 **infection**

860 (**A**) Triglyceride concentrations in PBS-injected and S.p.-infected flies with macrophage-specific ImpL2
861 knockdown (ImpL2^{RNAi}), overexpression (ImpL2^{CDS}) and their respective controls (TRiP^{control}, w^{1118}) at
862 whole-body level at 24 hpi. (**B-D**) Average size (**B**) and number (**C**) of lipid droplets and percentage of
863 area occupied (**D**) in the fat body of PBS-injected and S.p.-infected flies with macrophage-specific
864 ImpL2 knockdown (ImpL2^{RNAi}), overexpression (ImpL2^{CDS}) and their respective controls (TRiP^{control},
865 w^{1118}) at 24 hpi. (**E**) Representative confocal microscopy images of dissected fat body of PBS-injected
866 and S.p.-infected flies with macrophage-specific ImpL2 knockdown (ImpL2^{RNAi}), overexpression
867 (ImpL2^{CDS}) and their respective controls (TRiP^{control}, w^{1118}) at 24 hpi, stained with OilRedO (red), DAPI
868 (cyan) and phalloidin (white). The scale bar represents 20 µm. (**F**) Relative proportions of different
869 lipid species in the fat body of PBS-injected and S.p.-infected flies with macrophage-specific ImpL2
870 knockdown (ImpL2^{RNAi}), overexpression (ImpL2^{CDS}) and their respective controls (TRiP^{control}, w^{1118}) at
871 24 hpi. (**G**) Glycogen concentration in PBS-injected and S.p.-infected flies with macrophage-specific
872 ImpL2 knockdown (ImpL2^{RNAi}), overexpression (ImpL2^{CDS}) and their respective controls (TRiP^{control},
873 w^{1118}) at whole-body level at 24 hpi. Metabolite concentrations were normalized to the amount of
874 proteins in each sample and measured in three biological replicates. Values are mean ± SD, asterisks
875 mark statistically significant differences (*p<0.05; **p<0.01; ***p<0.001). (**B-D**) were quantified from
876 8 confocal microscopy images for each genotype and treatment, (**F**) lipidomic analysis was performed
877 in three biological replicates for each genotype and treatment. PC, phosphatidylcholine; PE,
878 phosphatidylethanolamine; TG, triglycerides; DG, diglycerides; PG, phosphatidylglycerol; PI,
879 phosphatidylinositol; LysoPC, Lyso-phosphatidylcholine; LysoPE, Lyso-phosphatidylethanolamine.

880

881 Figure 3. **Infection-induced autophagy and changes in gene expression in adipose tissue**

882 (**A**) Representative confocal microscopy images of fat body of control and infected flies with Atg8a-
883 mCherry autophagy reporter (Atg8a, red; DAPI, cyan). The scale bar represents 20 µm. (**B**) Graphical
884 representation of log2-fold change in mRNA expression of genes involved in insulin signaling,
885 lipoprotein and lipid metabolism, glycogenolysis and autophagy in the fat body of PBS-injected and
886 S.p.-infected flies with macrophage-specific ImpL2 knockdown (ImpL2^{RNAi}), overexpression (ImpL2^{CDS})
887 and their respective controls (TRiP^{control}, w^{1118}) at 24hpi. The first column (Infection) shows the log2-
888 fold change in mRNA expression in S.p-infected flies compared to Buff.-injected control flies (average
889 change for TRiP^{control} and w^{1118}). The second to fourth columns represent the log2-fold change in
890 mRNA expression compared to the corresponding control for knockdown (ImpL^{RNAi}/TRiP^{control}) and
891 overexpression (ImpL2^{CDS}/w^{1118}) in either uninfected (Buff.) or S.p. infected flies. Foxo, forkhead box
892 O; 4EBP, Thor; EIF-4E1, eukaryotic translation initiation factor 4E1; MTP, microsomal triacylglycerol
893 transfer protein; apoLPP, apolipophorin; apoLTP, apolipoprotein lipid transfer particle; Bmm,
894 brummer; Lip4, lipase 4; Hsl, hormone sensitive lipase; Glutaryl-CoA deh., Glutaryl-CoA
895 dehydrogenase; GlyS, glycogen synthase; GlyP, glycogen phosphorylase; Atg1, autophagy-related
896 gene 1; Atg6, autophagy-related gene 6.

897

898 Figure 3-figure supplement 1. **Expression levels of genes regulating metabolism in adipose tissue**

899 Gene expression of *Foxo, 4EBP, EIF4E1, GlutarylCoA deh., Lip4, apoLTP, apoLPP, MTP, Hsl, Bmm, GlyS,*
900 *GlyP, Atg1*, and *Atg6* genes in adipose tissue of flies injected with PBS (black bars) and infected with
901 *S. pneumoniae* (grey bars) with macrophage-specific ImpL2 knockdown, overexpression and their
902 respective controls; all genotypes depicted below the x-axis were crossed with *Hml>Gal4;*
903 *TubGal80^{TS}*. Expression levels normalized against rp49 are present as a fold-change relative to the
904 levels in the PBS-injected TRiP^{control}, which was arbitrarily set to 1. The individual dots represent
905 biological replicates. Values are mean ± SD, asterisks mark statistically significant differences
906 (*p<0.05; **p<0.01; ***p<0.001).

907

908 Figure 4. **Macrophage-derived ImpL2 affects adipose tissue metabolism via Foxo activity**

909 Representative confocal microscopy images of Foxo immunolocalization in the fat body of PBS-
910 injected and S.p.-infected flies with macrophage-specific ImpL2 knockdown (ImpL2^{RNAi}),
911 overexpression (ImpL2^{CDS}) and their respective controls (TRiP^{control}, w^{1118}) at 24 hpi; anti-dFoxo
912 antibody, green; DAPI, cyan. Histograms of Foxo cellular localization represent Foxo and DAPI signal
913 intensity in sections indicated by a white freehand line. The scale bar represents 20 µm.

914

915 Figure 5. **Macrophage-derived ImpL2 increases circulating carbohydrates and cholesterols to be**
916 **utilized by activated macrophages**

917 (**A-D**) Concentrations of circulating glucose (**A**), trehalose (**B**), cholesterol (**C**) and cholesteryl-ester (**D**)
918 in the hemolymph of PBS-injected and S.p.-infected flies with macrophage-specific ImpL2 knockdown
919 (ImpL2^{RNAi}), overexpression (ImpL2^{CDS}) and their respective controls (TRiP^{control}, w^{1118}) at 24 hpi. (**E-H**)
920 Concentrations of glucose (**E**), trehalose (**F**), cholesterol (**G**) and cholesteryl-ester (**H**) in hemocytes of
921 PBS-injected and S.p.-infected flies with macrophage-specific ImpL2 knockdown (ImpL2^{RNAi}),
922 overexpression (ImpL2^{CDS}), and their respective controls (TRiP^{control}, w^{1118}) at 24 hpi. (**I**) Proportional
923 occurrence of macrophages containing at least one lipid droplet (stained by OilRed O), counted in at
924 least fifty of Crq>GFP positive cells. (**J**) Representative confocal microscopy image of macrophages
925 (Crq>GFP) containing lipid droplets; neutral lipids were stained with OilRed O (red). The scale bar
926 represents 10 µm. The image represents a Z-stack consisting of a maximum projection of 5 layers. (**K**)
927 Representative confocal microscopy image depicting the ability of macrophage (Crq>GFP) to
928 endocytose lipoproteins (human LDL-pHrodo, red). The scale bar represents 13 µm. (**A-H**) Metabolite
929 concentrations were normalized to the amount of proteins in each sample. Metabolic measurements
930 were performed in three biological replicates. Values are mean ± SD, asterisks mark statistically
931 significant differences (*p<0.05; **p<0.01; ***p<0.001).

932

933 Figure 6. **Macrophage-derived ImpL2 is important for resistance to bacterial infection**

934 (**A, C**) Survival rate of S.p.-infected and PBS-injected flies with macrophage-specific ImpL2 knockdown
935 (ImpL2^{RNAi}) (**A**), overexpression (ImpL2^{CDS}) (**C**) and their respective controls (TRiP^{control}, w^{1118}). Three
936 independent experiments were performed and combined into one survival curve; the number of
937 individuals per replicate was at least 500 for each genotype. (**B, D**) Pathogen load in S.p.-infected and
938 PBS-injected flies with knockdown (ImpL2^{RNAi}) (**B**), overexpression (ImpL2^{CDS}) (**D**) and their respective
939 controls (TRiP^{control}, w^{1118}) at 24 and 48 hpi. The individual dots in the plot represent the number of

940 bacteria (colony forming units-CFUs) in one fly. The data show results combined from three
941 independent biological replicates. (**E**) Confocal microscopy image depicting the ability of a
942 macrophage (Crq>GFP) to phagocytose an invading pathogen (*S. aureus*-pHrodo-red). The scale bar
943 represents 10 µm. The image represents a Z-stack consisting of a maximum projection of 5 layers. (**F**)
944 Phagocytic rate calculated for S.p.-infected flies with knockdown (ImpL2^{RNAi}), overexpression
945 (ImpL2^{CDS}), and their respective controls (TRiP^{control}, w^{1118}); each dot in the plot represents the
946 number of phagocytic events per macrophage (Crq>GFP). The results are combined from three
947 biological replicates. Values are mean ± SD, asterisks mark statistically significant differences
948 (*p<0.05; **p<0.01; ***p<0.001).

949

950 Figure 7. **Maladaptive effects of ImpL2 when overexpressed during development and in chronic**
951 **infection**

952 (**A**) Representative images of a developmental defect of the dorsal closure in the abdomen of a fly
953 with macrophage-specific ImpL2 overexpression throughout development (Crq>Gal4>ImpL2^{CDS}) (left),
954 and melanized spots in a fly with temporal (48 hours), macrophage-specific ImpL2 overexpression
955 (Hml>Gal4; Gal80^{TS}>ImpL2^{CDS}) (middle), with the aortic region (upper right with arrows pointing to
956 melanized spots) and melanized spot (lower right) at higher magnification. (**B, D**) Survival rate of *L.*
957 *monocytogenes*-infected and PBS-injected flies with macrophage-specific ImpL2 knockdown
958 (ImpL2^{RNAi}) (**B**), overexpression (ImpL2^{CDS}) (**D**) and their respective controls (TRiP^{control}, w^{1118}). Three
959 independent experiments were performed and combined into each survival curve; the number of
960 individuals per replicate was at least 500 for each genotype. (**C, E**) Pathogen load of *L.*
961 *monocytogenes* in flies with macrophage-specific ImpL2 knockdown (ImpL2^{RNAi}) (**C**), overexpression
962 (ImpL2^{CDS}) (**E**) and their respective controls (TRiP^{control}, w^{1118}) shownas either total load or only
963 intracellular *Listeria* subpopulation at 24 hpi and at 12 days post-infection. The individual dots in the
964 plot represent the number of bacteria (colony forming units-CFUs) in one fly. The data show results
965 combined from three independent biological replicates. Values are mean ± SD, asterisks mark
966 statistically significant differences (*p<0.05; **p<0.01; ***p<0.001).

967

968 Figure 8. **IGFBP7, the mammalian homolog of ImpL2, is produced in human macrophages in**
969 **response to *S. pneumoniae in vitro***

970 (**A**) Confocal microscopy images of PMA-activated control THP-1 cells (left) and PMA-activated THP-1
971 cells actively interacting with GFP-labeled *S. pneumoniae* (green) *in vitro* (right). The scale bar
972 represents 10 µm. The image on the right is a maximum projection of 3 layers. (**B**) Gene expression of
973 IGFBP7, IGFBP3 and IGFBP4 in PMA-activated THP-1 cells 24 hours after exposure to *S. pneumoniae*
974 *in vitro*. Expression levels normalized against ACTB are shown as a fold change relative to levels of
975 IGFBP7 in controls that were arbitrarily set to 1. Values are mean ± SD, asterisks mark statistically
976 significant differences (*p<0.05; **p<0.01; ***p<0.001).

977

978 Figure 9. **Schematic representation of the proposed model of ImpL2 function during infection**

979 Upon recognition of the bacteria, the macrophages switch to Hif1α-driven aerobic glycolysis. Hif1α
980 also induces the expression of the ImpL2-RA isoform by binding to hypoxia response elements in the
981 promotor of the ImpL2 gene. Macrophage-derived ImpL2 then remotely activates Foxo re-
982 localization to the nucleus in the fat body, leading to the expression of metabolic Foxo-target genes.

983 Mobilized sources, manifested by hyperlipidemia and hyperglycemia in the hemolymph, are
984 subsequently used by activated macrophages. These transient changes in ImpL2-regulated
985 metabolism are essential for efficient bacterial killing and resistance to infection. However, if
986 prolonged, for example during chronic infection, macrophage-derived ImpL2 can harm the host by
987 potential wasting. Hif1α, hypoxia-inducible factor 1 α; HREs, hypoxia response elements; ImpL2,
988 imaginal morphogenesis protein-late 2; Foxo, forkhead box O.

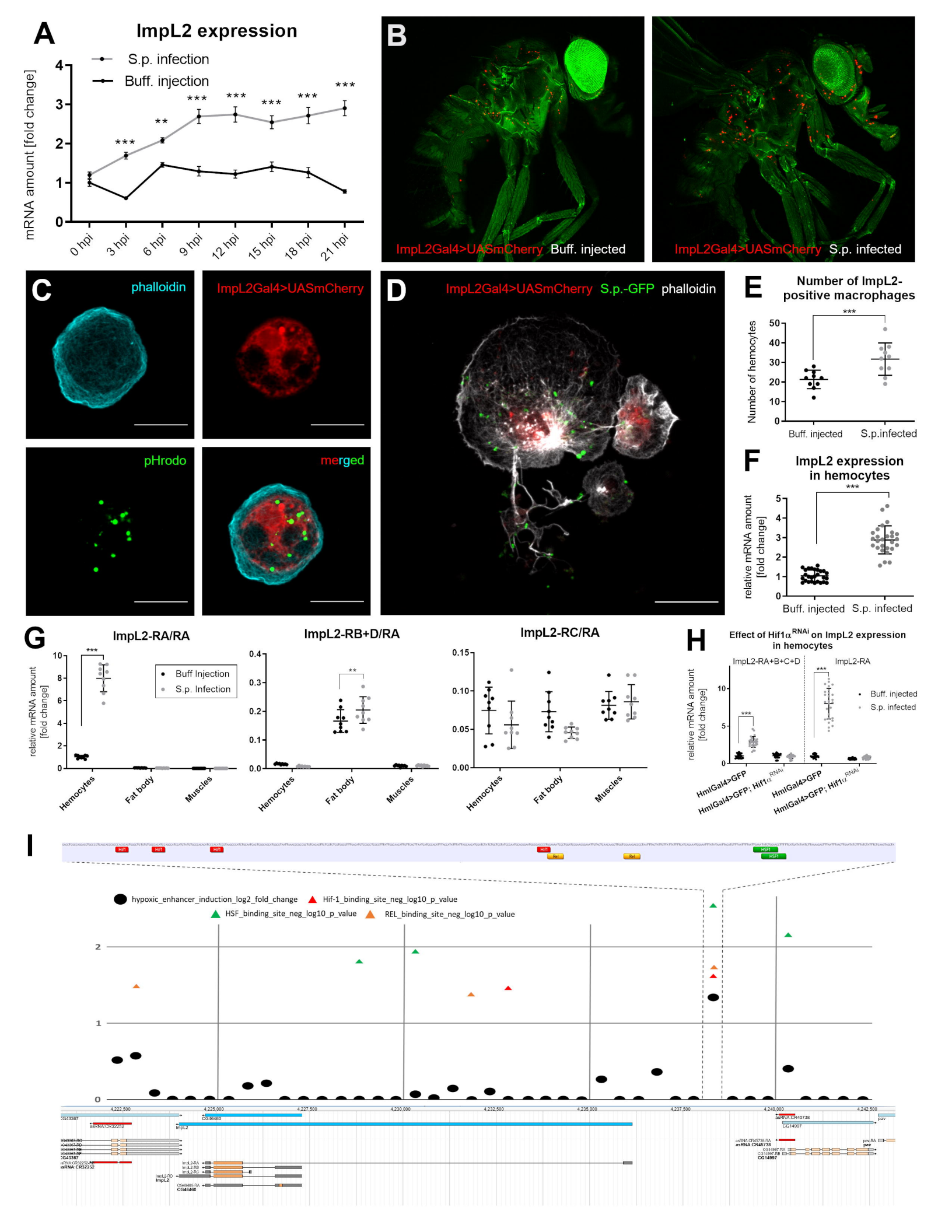
A
ImpL2 expression
S.p. infection
Buff. injection
mRNA amount [fold change]
0 hpi
3 hpi
6 hpi
9 hpi
12 hpi
15 hpi
18 hpi
21 hpi
B
ImpL2Gal4>UASmCherry Buff. injected
ImpL2Gal4>UASmCherry S.p. infected
C
phalloidin
ImpL2Gal4>UASmCherry
pHrodo
merged
D
ImpL2Gal4>UASmCherry S.p.-GFP phalloidin
E
Number of ImpL2-positive macrophages
Number of hemocytes
Buff. injected
S.p.infected
F
ImpL2 expression in hemocytes
relative mRNA amount [fold change]
Buff. injected
S.p. infected
G
ImpL2-RA/RA
ImpL2-RB+D/RA
ImpL2-RC/RA
relative mRNA amount [fold change]
Buff Injection
S.p. Infection
Hemocytes
Fat body
Muscles
H
Effect of Hif1α RNAi on ImpL2 expression in hemocytes
ImpL2-RA+B+C+D
ImpL2-RA
relative mRNA amount [fold change]
Buff. injected
S.p. infected
HmlGal4>GFP
HmlGal4>GFP; Hif1α RNAi
I
hypoxic_enhancer_induction_log2_fold_change
Hif-1_binding_site_neg_log10_p_value
HSF_binding_site_neg_log10_p_value
REL_binding_site_neg_log10_p_value

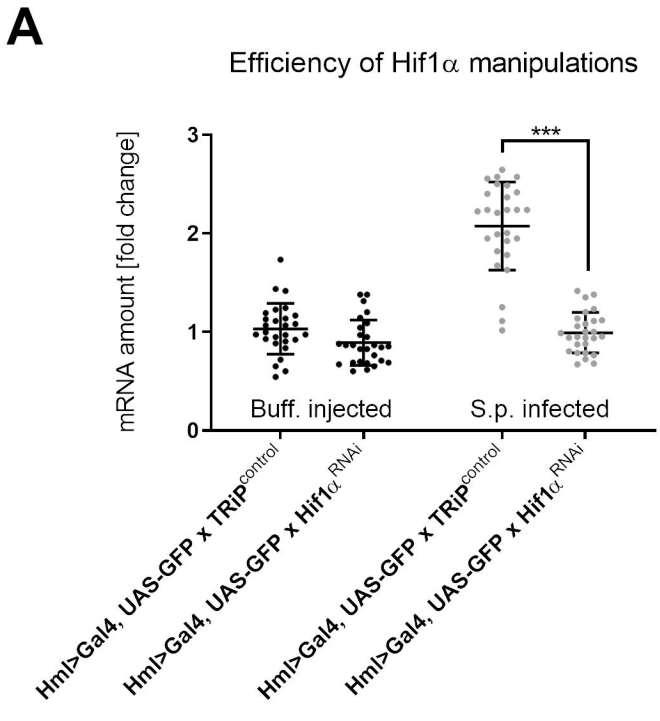
A
Efficiency of Hif1α manipulations
mRNA amount [fold change]
3
2
1
0
***
Buff. injected
S.p. infected
Hml>Gal4, UAS-GFP x TRiP^control
Hml>Gal4, UAS-GFP x Hif1α^RNAi
Hml>Gal4, UAS-GFP x TRiP^control
Hml>Gal4, UAS-GFP x Hif1α^RNAi

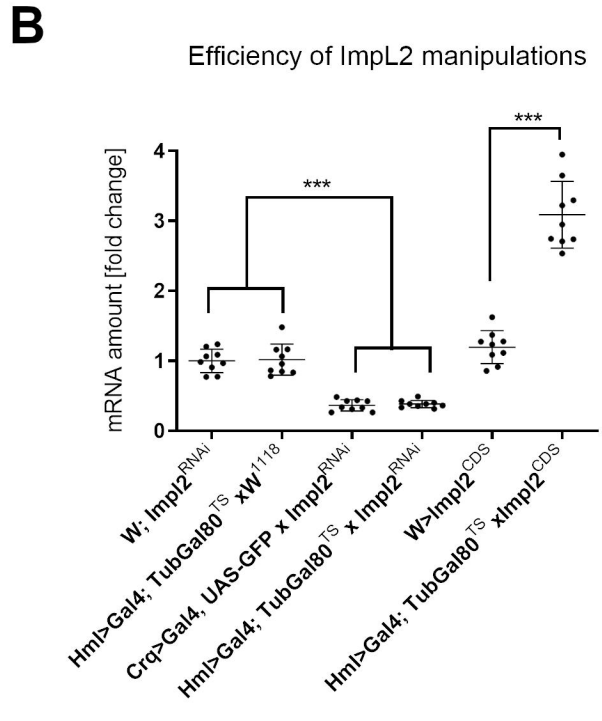
B
Efficiency of ImpL2 manipulations
mRNA amount [fold change]
4
3
2
1
0
***
***
W; Impl2^RNAi
Hml>Gal4; TubGal80^TS xW^1118
Hml>Gal4; TubGal80^TS x Impl2^RNAi
Crq>Gal4, UAS-GFP x Impl2^RNAi
W>Impl2^CDS
Hml>Gal4; TubGal80^TS xImpl2^CDS

ImpL2-RA regulatory sequence:

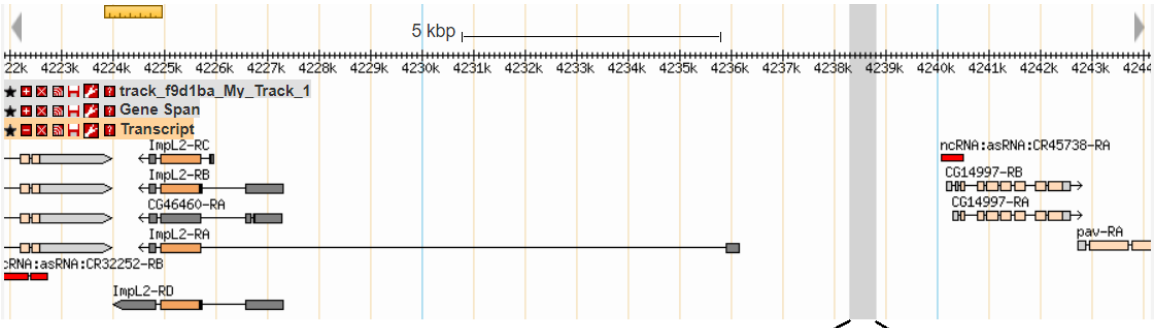

sequence:

GACCTCGCCAGGACCTGCCCCTCAGCACCCGCCCACGCAGTGGGCTGTGTG

TGGCCACATCCAGCCATCCATCTATGTGCCCACACATCCCACATCCGTAAG

CCCATCTGCAATCAGTCGGCAGCATGGCGTAATTAAACCCGCCGCTGTCAC

AGTTGTCGTCTCGTGGCGTTTGACATGTCCGCCTCGCGTTTATTGGCAACA

TTGTTCACTTAATCATCCCACATTTACCATATTTATTAGCAACATCGATCT

ATCTGCTCGTATCCGAATGCACGGAATGGGGAGCCGTGGAAAATCCCTGGA

TCCGAAGGGAAATTGTACTCAACAAGCTTGGTGGAAAGACCCCTAATTTAC

TATTGTTATTATTTTCATCAGAAATCGAAATTTATATAAATTACATGTTTA

ATTTTAATTGAAATATCTGGAACCTTTTTCATGATATAATCTTAAAAGAGT

TTAATTTAACTTGAATATCTTTATCTATTTCTGAAGTAGCTA

Hif1-α binding site Rel binding site HSF binding site

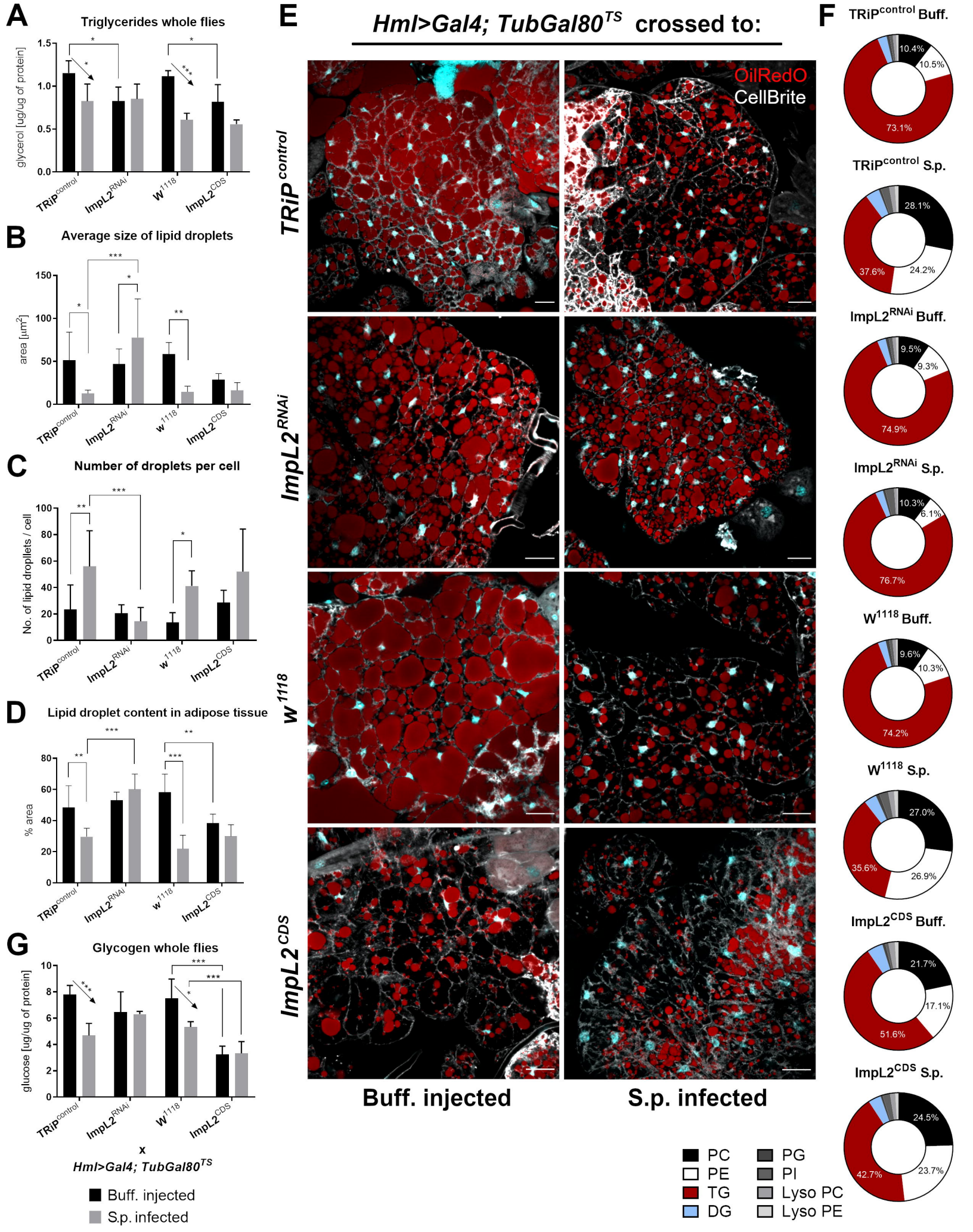
A
Triglycerides whole flies
glycerol [ug/ug of protein]
TRiP^control
ImpL2^RNAi
W^1118
ImpL2^CDS
B
Average size of lipid droplets
area [µm²]
C
Number of droplets per cell
No. of lipid droplets / cell
D
Lipid droplet content in adipose tissue
% area
G
Glycogen whole flies
glucose [ug/ug of protein]
x
Hml>Gal4; TubGal80^TS
Buff. injected
S.p. infected
E
Hml>Gal4; TubGal80^TS crossed to:
TRiP^control
ImpL2^RNAi
W^1118
ImpL2^CDS
OilRedO
CellBrite
Buff. injected
S.p. infected
F
TRiP^control Buff.
10.4%
10.5%
73.1%
TRiP^control S.p.
28.1%
37.6%
24.2%
ImpL2^RNAi Buff.
9.5%
9.3%
74.9%
ImpL2^RNAi S.p.
10.3%
6.1%
76.7%
W^1118 Buff.
9.6%
10.3%
74.2%
W^1118 S.p.
27.0%
35.6%
26.9%
ImpL2^CDS Buff.
21.7%
17.1%
51.6%
ImpL2^CDS S.p.
24.5%
42.7%
23.7%
PC
PE
TG
DG
PG
PI
Lyso PC
Lyso PE

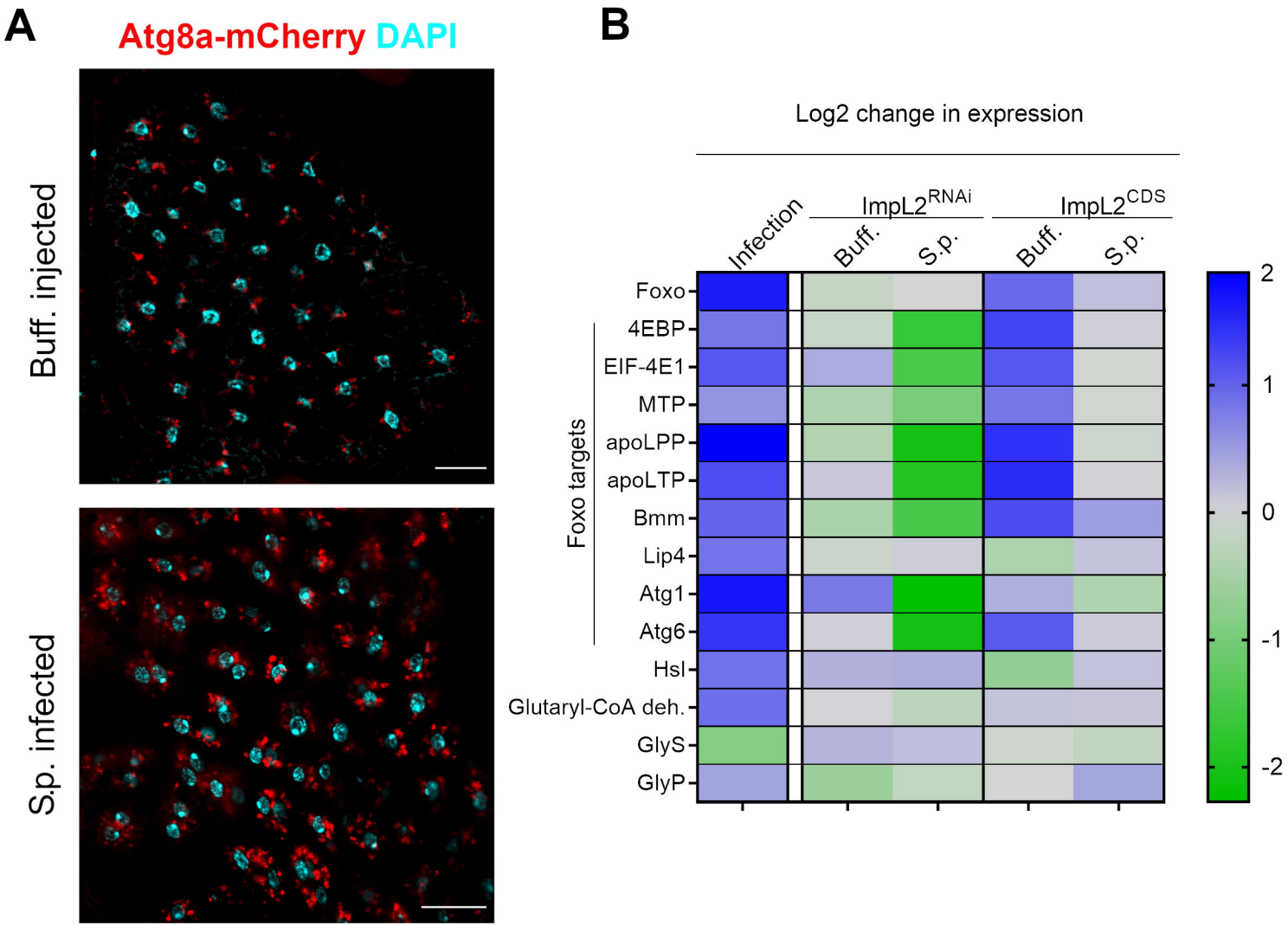
A
Atg8a-mCherry DAPI
Buff. injected
S.p. infected
B
Log2 change in expression
Infection
ImpL2RNAi
ImpL2CDS
Buff.
S.p.
Buff.
S.p.
Foxo
4EBP
EIF-4E1
MTP
apoLPP
apoLTP
Bmm
Lip4
Atg1
Atg6
Hsl
Glutaryl-CoA deh.
GlyS
GlyP
Foxo targets
2
1
0
-1
-2

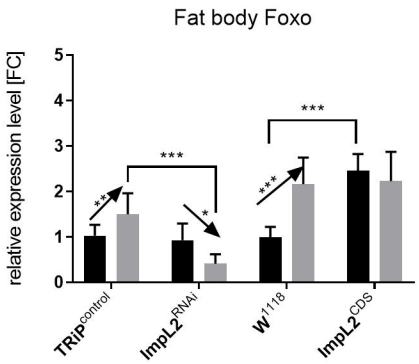
Fat body Foxo
relative expression level [FC]
TRiP^control
ImpL2^RNAi
w^1118
ImpL2^CDS

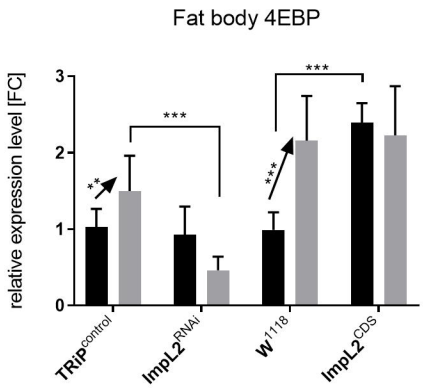
Fat body 4EBP
relative expression level [FC]
TRiP^control
ImpL2^RNAi
w^1118
ImpL2^CDS

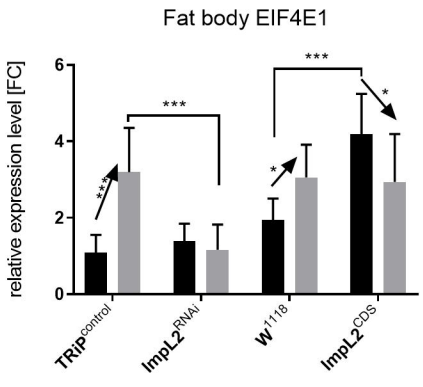
Fat body EIF4E1
relative expression level [FC]
TRiP^control
ImpL2^RNAi
w^1118
ImpL2^CDS

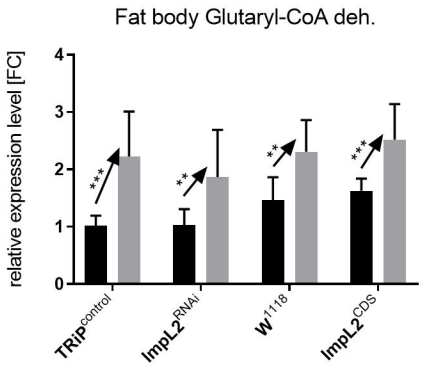
Fat body Glutaryl-CoA deh.
relative expression level [FC]
TRiP^control
ImpL2^RNAi
w^1118
ImpL2^CDS

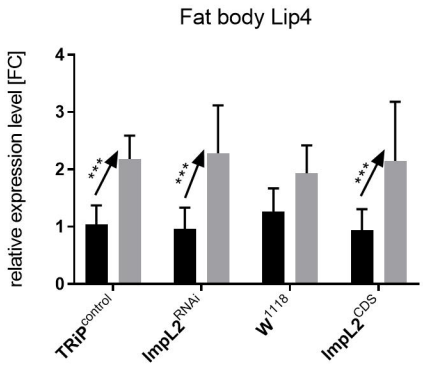
Fat body Lip4
relative expression level [FC]
TRiP^control
ImpL2^RNAi
w^1118
ImpL2^CDS

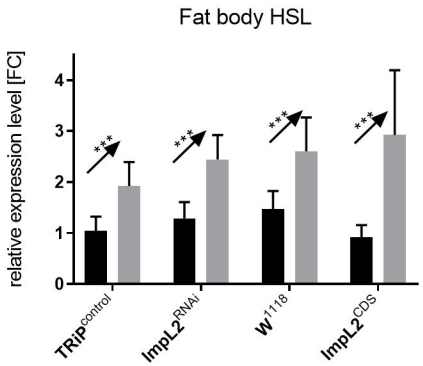
Fat body HSL
relative expression level [FC]
TRiP^control
ImpL2^RNAi
w^1118
ImpL2^CDS

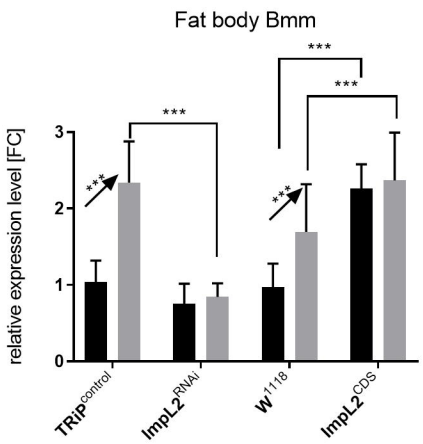
Fat body Bmm
relative expression level [FC]
TRiP^control
ImpL2^RNAi
w^1118
ImpL2^CDS

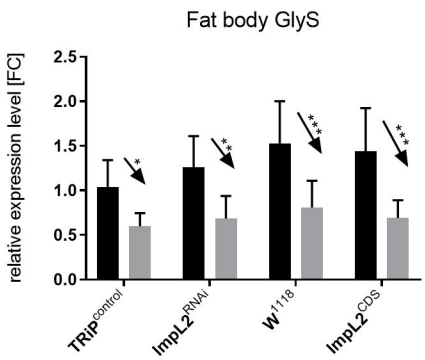
Fat body GlyS
relative expression level [FC]
TRiP^control
ImpL2^RNAi
w^1118
ImpL2^CDS

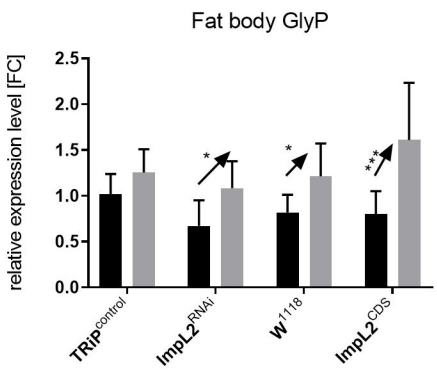
Fat body GlyP
relative expression level [FC]
TRiP^control
ImpL2^RNAi
w^1118
ImpL2^CDS

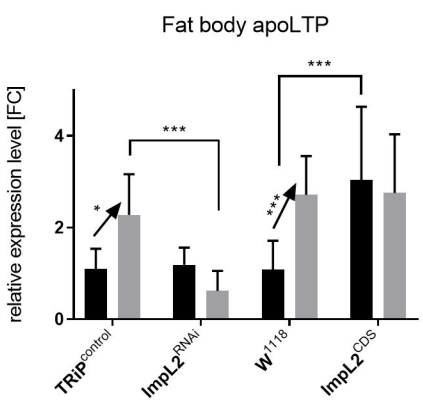
Fat body apoLTP
relative expression level [FC]
TRiP^control
ImpL2^RNAi
w^1118
ImpL2^CDS

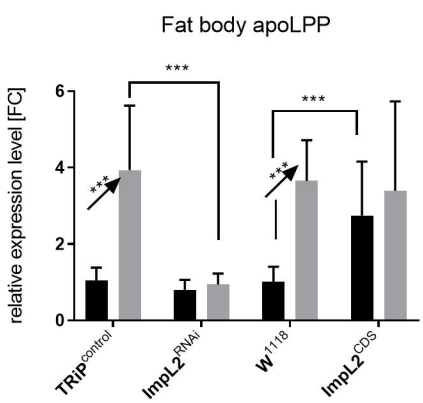
Fat body apoLPP
relative expression level [FC]
TRiP^control
ImpL2^RNAi
w^1118
ImpL2^CDS

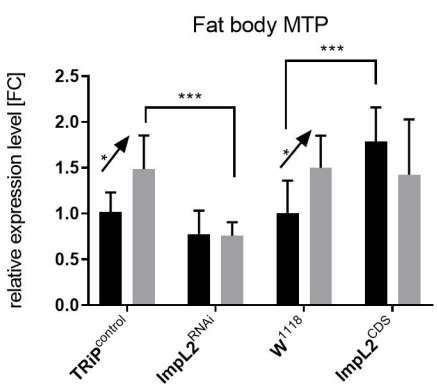
Fat body MTP
relative expression level [FC]
TRiP^control
ImpL2^RNAi
w^1118
ImpL2^CDS

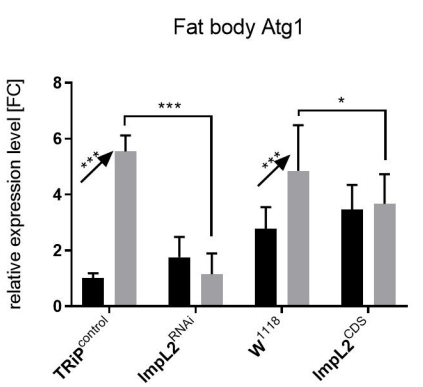
Fat body Atg1
relative expression level [FC]
TRiP^control
ImpL2^RNAi
w^1118
ImpL2^CDS

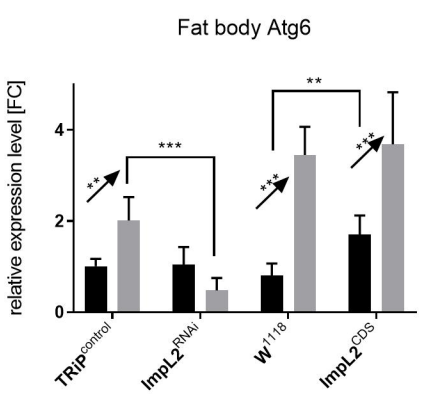
Fat body Atg6
relative expression level [FC]
TRiP^control
ImpL2^RNAi
w^1118
ImpL2^CDS

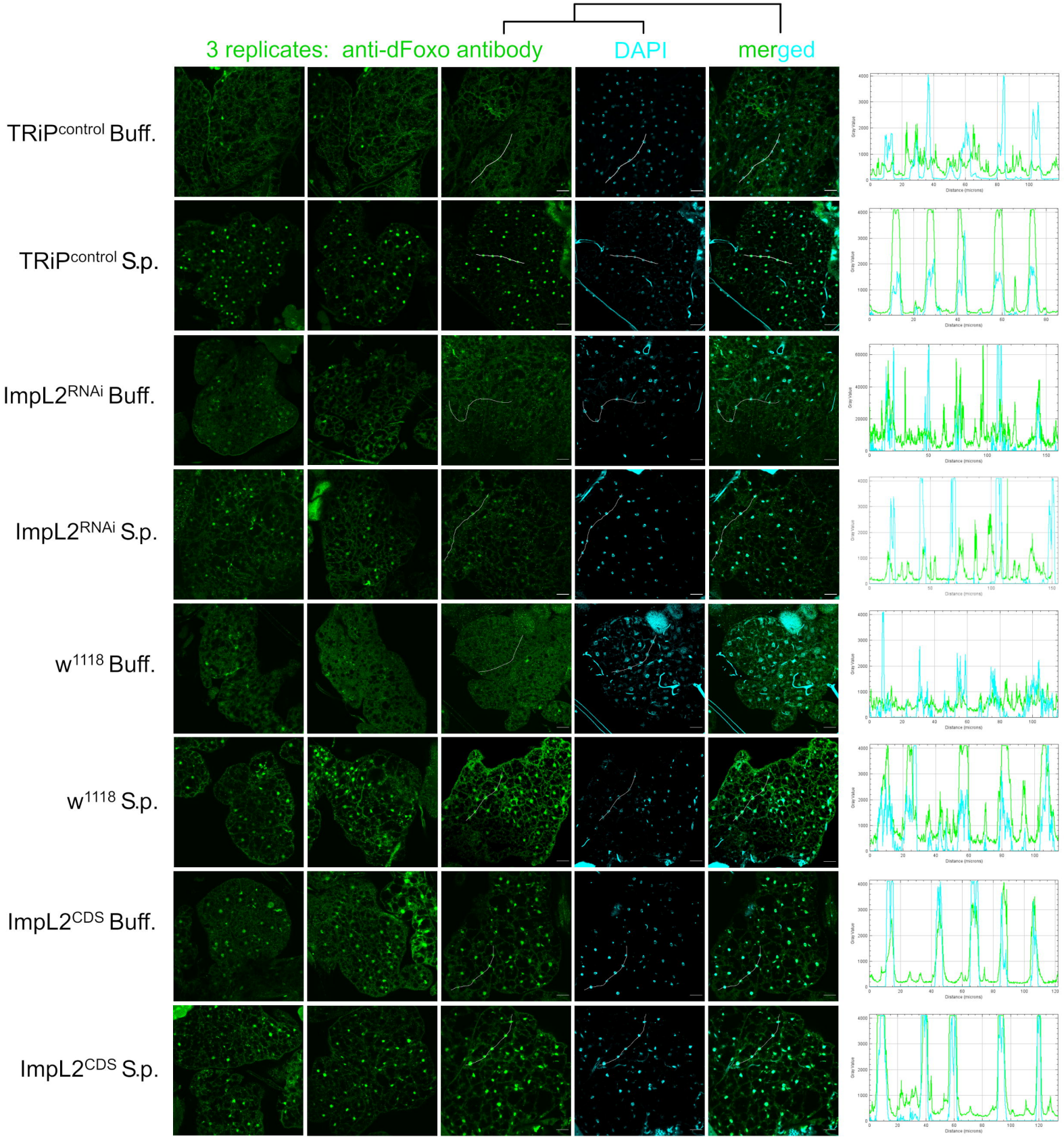
3 replicates: anti-dFoxo antibody
DAPI
merged
TRiP^control Buff.
TRiP^control S.p.
ImpL2^RNAi Buff.
ImpL2^RNAi S.p.
w^1118 Buff.
w^1118 S.p.
ImpL2^CDS Buff.
ImpL2^CDS S.p.
Gray Value
Distance (microns)

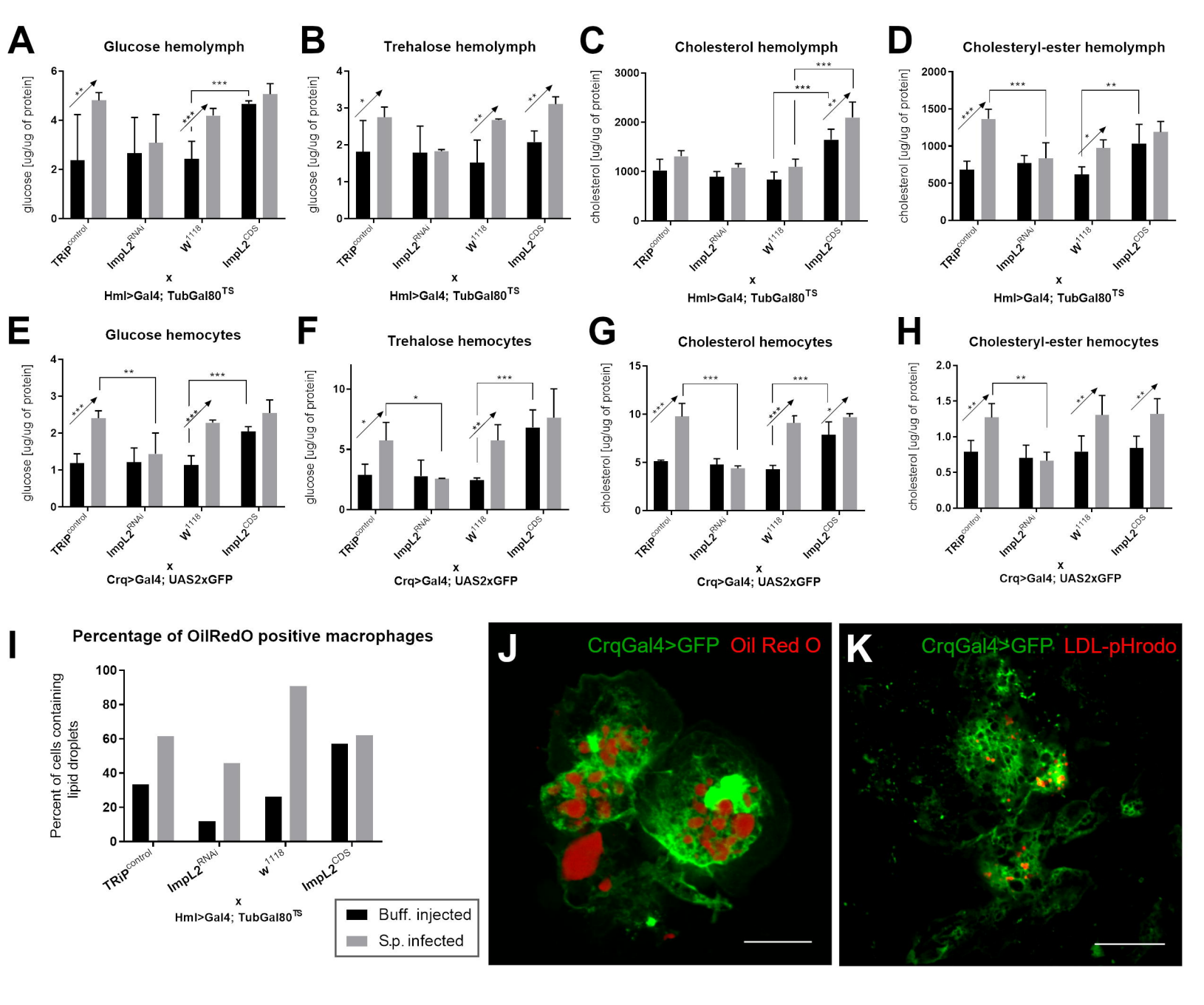
A
Glucose hemolymph
glucose [ug/ug of protein]
TRiP^control
ImpL2^RNAi
w^1118
ImpL2^CDS
x
Hml>Gal4; TubGal80^TS
B
Trehalose hemolymph
glucose [ug/ug of protein]
C
Cholesterol hemolymph
cholesterol [ug/ug of protein]
D
Cholesteryl-ester hemolymph
cholesterol [ug/ug of protein]
E
Glucose hemocytes
glucose [ug/ug of protein]
Crq>Gal4; UAS2xGFP
F
Trehalose hemocytes
glucose [ug/ug of protein]
G
Cholesterol hemocytes
cholesterol [ug/ug of protein]
H
Cholesteryl-ester hemocytes
cholesterol [ug/ug of protein]
I
Percentage of OilRedO positive macrophages
Percent of cells containing lipid droplets
Buff. injected
S.p. infected
J
CrqGal4>GFP Oil Red O
K
CrqGal4>GFP LDL-pHrodo

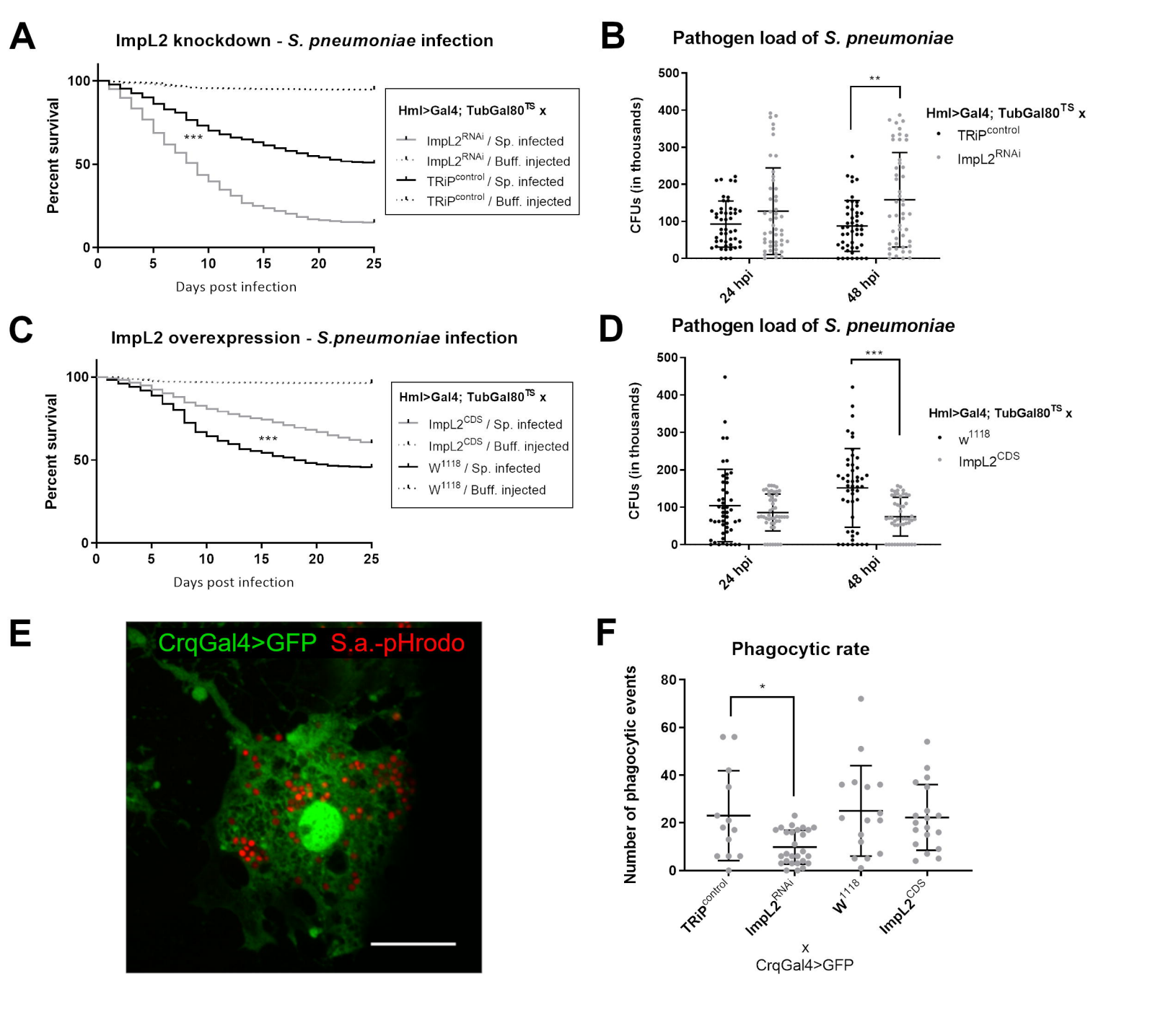
A
ImpL2 knockdown - S. pneumoniae infection
Percent survival
Days post infection
***
Hml>Gal4; TubGal80TS x
ImpL2RNAi / Sp. infected
ImpL2RNAi / Buff. injected
TRiPcontrol / Sp. infected
TRiPcontrol / Buff. injected
B
Pathogen load of S. pneumoniae
CFUs (in thousands)
**
24 hpi
48 hpi
Hml>Gal4; TubGal80TS x
TRiPcontrol
ImpL2RNAi
C
ImpL2 overexpression - S.pneumoniae infection
Percent survival
Days post infection
***
Hml>Gal4; TubGal80TS x
ImpL2CDS / Sp. infected
ImpL2CDS / Buff. injected
W1118 / Sp. infected
W1118 / Buff. injected
D
Pathogen load of S. pneumoniae
CFUs (in thousands)
***
24 hpi
48 hpi
Hml>Gal4; TubGal80TS x
W1118
ImpL2CDS
E
CrqGal4>GFP S.a.-pHrodo
F
Phagocytic rate
Number of phagocytic events
*
TRiPcontrol
ImpL2RNAi
W1118
ImpL2CDS
x
CrqGal4>GFP

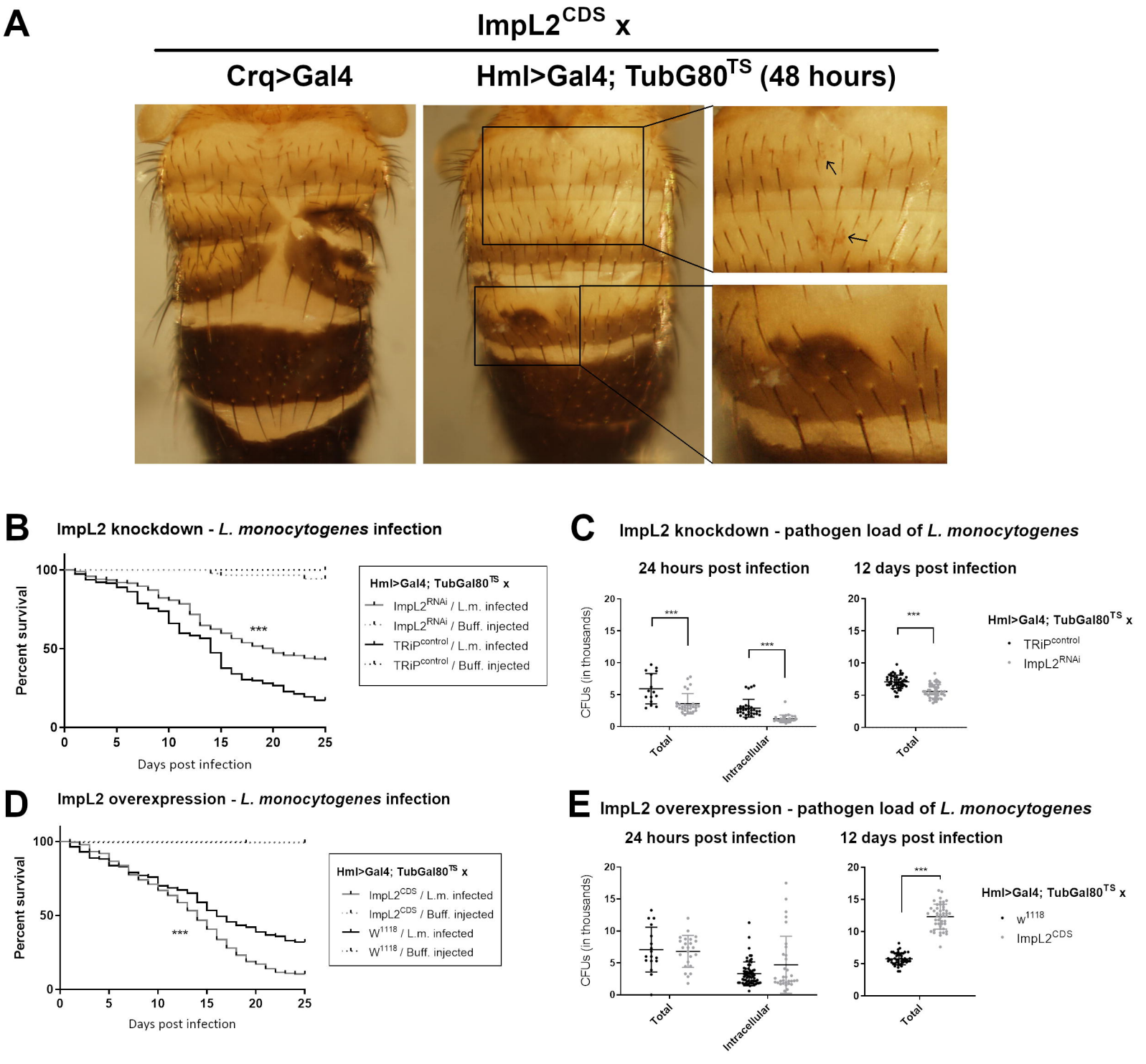
A
ImpL2CDS x
Crq>Gal4
Hml>Gal4; TubG80TS (48 hours)
B
ImpL2 knockdown - L. monocytogenes infection
Percent survival
Days post infection
***
Hml>Gal4; TubGal80TS x
ImpL2RNAi / L.m. infected
ImpL2RNAi / Buff. injected
TRiPcontrol / L.m. infected
TRiPcontrol / Buff. injected
C
ImpL2 knockdown - pathogen load of L. monocytogenes
24 hours post infection
12 days post infection
CFUs (in thousands)
Total
Intracellular
Hml>Gal4; TubGal80TS x
TRiPcontrol
ImpL2RNAi
D
ImpL2 overexpression - L. monocytogenes infection
Percent survival
Days post infection
Hml>Gal4; TubGal80TS x
ImpL2CDS / L.m. infected
ImpL2CDS / Buff. injected
W1118 / L.m. infected
W1118 / Buff. injected
E
ImpL2 overexpression - pathogen load of L. monocytogenes
24 hours post infection
12 days post infection
CFUs (in thousands)
Total
Intracellular
Hml>Gal4; TubGal80TS x
W1118
ImpL2CDS

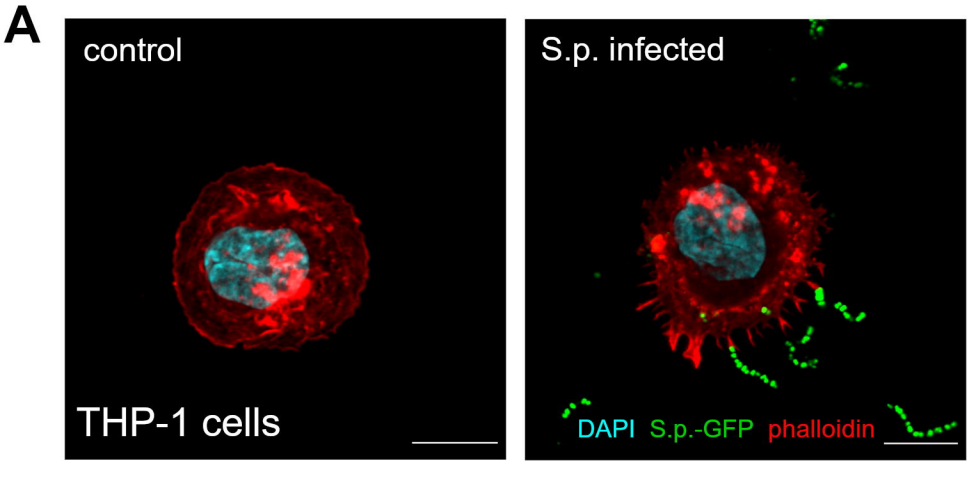
A
control
THP-1 cells
S.p. infected
DAPI S.p.-GFP phalloidin

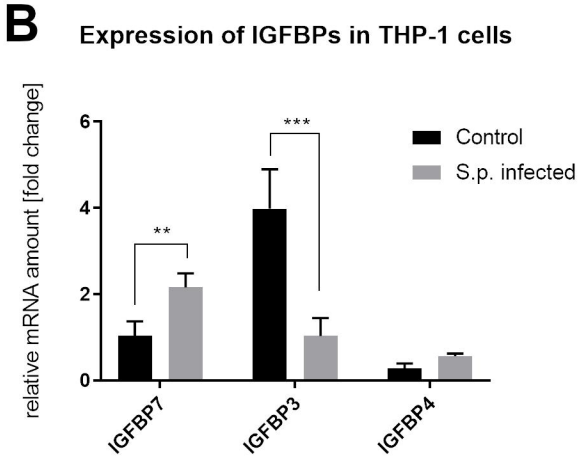
B
Expression of IGFBPs in THP-1 cells
relative mRNA amount [fold change]
6
4
2
0
**
***
Control
S.p. infected
IGFBP7
IGFBP3
IGFBP4

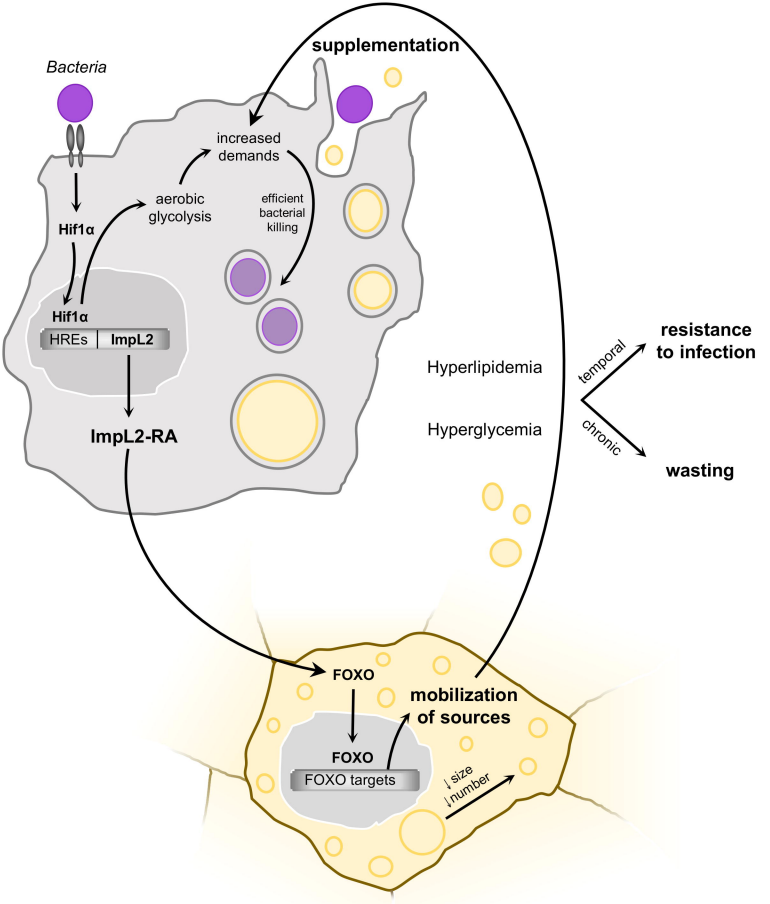
Bacteria
supplementation
increased demands
aerobic glycolysis
efficient bacterial killing
Hif1α
Hif1α
HREs
ImpL2
ImpL2-RA
Hyperlipidemia
Hyperglycemia
temporal
chronic
resistance to infection
wasting
FOXO
FOXO
FOXO targets
mobilization of sources
↓size
↓number